AGU Advances

Supporting Information for

Decadal Trends in the Oceanic Storage of Anthropogenic Carbon from 1994 to 2014

Jens Daniel Müller[1], N. Gruber[1], B. Carter[2,3], R. Feely[3], M. Ishii[4], N. Lange[5], S.K. Lauvset[6], A. Murata[7], A. Olsen[8], F.F. Pérez[9,10], C. Sabine[12], T. Tanhua[5], R. Wanninkhof[13], D. Zhu[1]

[1]Environmental Physics, Institute of Biogeochemistry and Pollutant Dynamics, ETH Zurich, Zurich, Switzerland.
[2]Cooperative Institute for Climate, Ocean, and Ecosystem Studies, University of Washington, Seattle, WA, 98105.
[3]Pacific Marine Environmental Laboratory, National Oceanic and Atmospheric Administration, Seattle, WA, 98115.
[4]Meteorological Research Institute, Japan Meteorological Agency, Tsukuba, Japan.
[5]GEOMAR Helmholtz Centre for Ocean Research Kiel, Kiel, Germany.
[6]NORCE Norwegian Research Centre, Bjerknes Centre for Climate Research, Bergen, Norway.
[7]Japan Agency for Marine-Earth Science and Technology, Yokosuka, Kanagawa, 237-0061, Japan.
[8]Geophysical Institute, University of Bergen and Bjerknes Centre for Climate Research, Bergen, Norway.
[9]Instituto de Investigaciones Marinas (IIM), CSIC, Vigo, Spain.
[10]Oceans Department, Stanford University, Stanford, CA 94305, USA.
[12]University of Hawaii at Manoa, Honolulu, HI, 96822.
[13]Atlantic Oceanographic and Meteorological Laboratory, National Oceanographic and Atmospheric Administration, Miami, USA.

Contents of this file

Text S1 to S6
Figures S1 to S19
Table S1

Introduction

In this supplement we provide supporting information about the observational data base underlying our results (S1), with a particular focus on adjustments that we applied to improve the data consistency (S1.2). We provide information about the exact configuration of our statistical method, discussing also aspects of the configuration that we tested during this study, but that revealed to be of secondary relevance (S2). We provide additional observation-based results to extend the information given in the main text (S3). In section S4, a detailed description of our uncertainty and sensitivity assessment is given, including also a decomposition of the uncertainty into its components. We extend this uncertainty assessment in section S5 through reporting the results of our tests of the eMLR(C*) method with synthetic data from a Global Ocean Biogeochemical Model (GOBM). Finally, we provide a detailed comparison of our results to those obtained from previous regional studies (S6).

S1 Observational data base

S1.1 Basin mask for regional clustering

Based on the basin mask provided by the World Ocean Atlas 2018 (Garcia et al., 2019), we derived six different definitions (Fig. S1) of the main ocean basins that we used to cluster the data in the horizontal dimensions for the eMLR(C*) analysis.

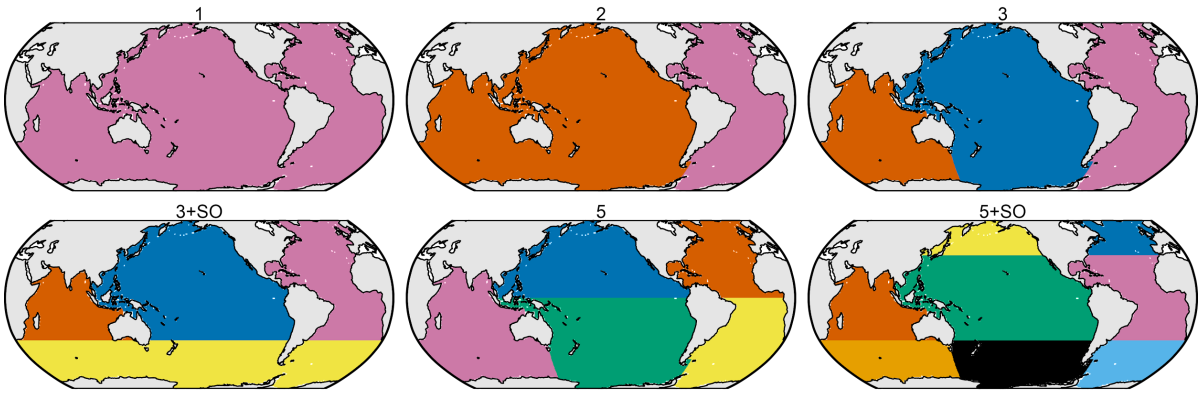

Fig. S1: The six basin mask definitions used to cluster observations for the fitting of MLR models and the subsequent mapping of ΔC_{ant}. Basin mask "3" was used for our standard case reconstructions of ΔC_{ant}. Basin mask "5" was also used to integrate ΔC_{ant} inventories for individual ocean basins.

S1.2 Data adjustments for the Indian Ocean and North Pacific

A prerequisite for the accurate reconstruction of ΔC_{ant} is the consistency of the underlying measurements. In this regard, the eMRL(C*) method profits from the incorporation of all available cruise data from one sampling period in a single model fitting step, which reduces the sensitivity to measurement biases, which are often attributed to different instrumental set-ups, procedures or staff on individual cruises. Furthermore, GLODAP performs a comprehensive data quality assessment and reduces remaining biases when compiling observations into a harmonised database. This is achieved through data adjustments based on crossover comparisons of deep water measurements. The ambitious aim of GLODAP is to provide an overall consistent data set comprising observations collected over more than five decades (Lauvset et al., 2021; Olsen et al., 2016).

Despite these efforts, applying the eMLR(C*) method to observations as published in GLODAPv2.2021, leads to an evenly distributed ΔC_{ant} signal below 1500m that is in the order of +3 µmol kg^{-1} in the Indian Ocean for the 1994–2004 period and in the order of +2 µmol kg^{-1} in the North Pacific Ocean for the 2004–2014 period (Fig. S2). This deep water ΔC_{ant} accumulation causes substantially (regionally up to 10 mol m^{-2} dec^{-1}) elevated column inventory changes in the two hemispheric basins (Fig. S11). Such a strong accumulation of ΔC_{ant} in the deep waters of these basins cannot be reasonably explained based on oceanographic knowledge and is further in disagreement with the close-to-zero levels of pCFC-12 (Key et al., 2004) and total C_{ant} (Sabine et al., 2004) estimated for these water masses in 1994. Likewise, we do not find a similar deep water ΔC_{ant} increase in the respective other decade, i.e. the 2004–2014 period for the Indian and the 1994–2004 period

for the Pacific Ocean. Extensive configuration changes and tests of the eMLR(C*) method (including the separate analysis of 20° latitude or longitude bands, the removal of individual predictors, the use of DIC as target variable, and using reoccupied cruises only) indicate that the elevated deep water ΔC_{ant} signal in these two regions is not causes by a methodological artefact.

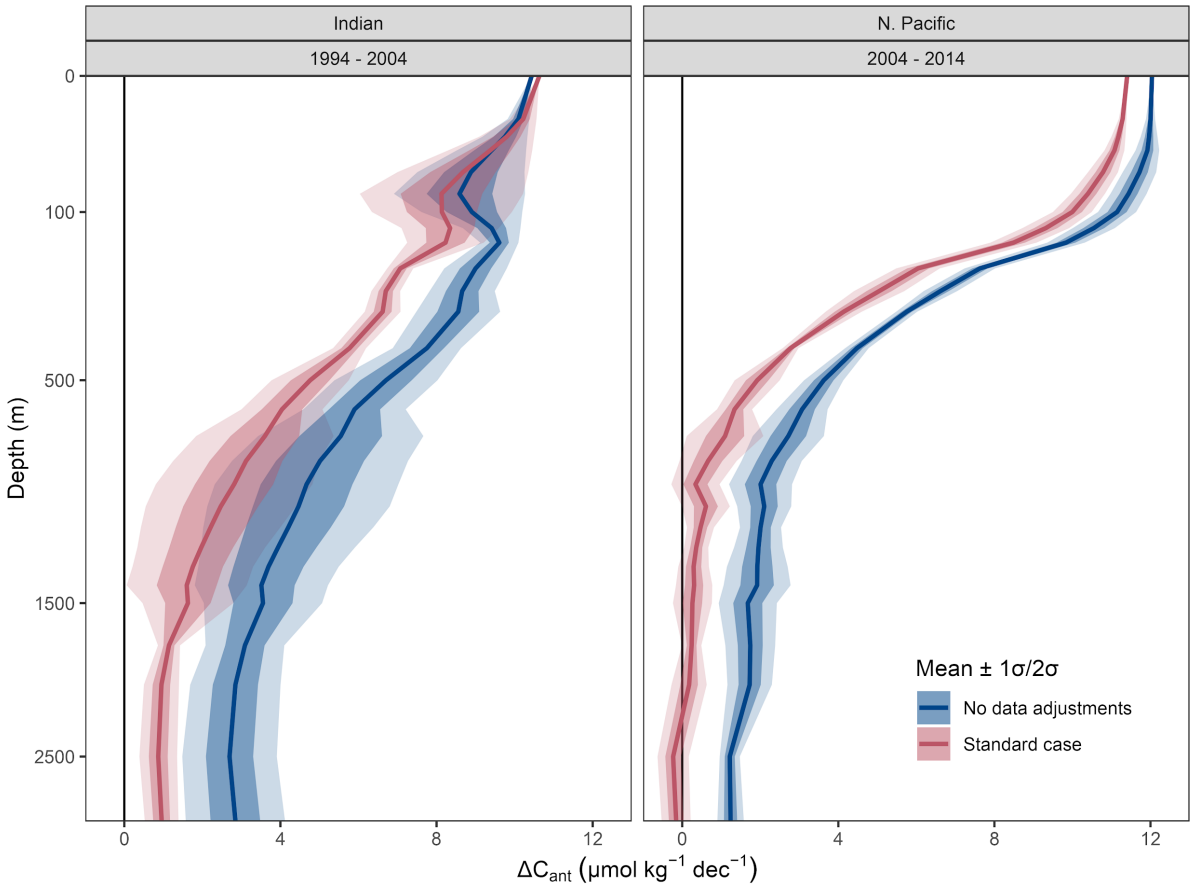

Fig. S2: ΔC_{ant} profiles determined with the eMLR(C*) method applied to adjusted (blue) and unadjusted (red) data, for 1994–2004 in the Indian Ocean (left) and for 2004–2014 in the North Pacific (right). The solid lines refer to the reconstructions based on the standard basin clustering scheme "3", while the ribbons indicate 1 and 2 standard deviations across the reconstructions of all 6 basin clustering options displayed in Fig. S1.

In contrast, several lines of arguments suggest a bias in the underlying observations. An evaluation of the GLODAP crossover results (Olsen et al., 2016 and subsequent GLODAP updates) revealed remaining mean decade-to-decade offsets expressed in C* units in the adjusted GLODAP products of around +5 μmol kg^{-1} when comparing the RV Knorr Indian Ocean cruises from the 2000s and the 1990s, and of around +3 μmol kg^{-1} when comparing all North Pacific Ocean cruises from the 2010s and the 2000s (Fig. S3). The offsets in C* units represent the sum of the content offsets in DIC, TA and phosphate, the last of which was approximated as the product of the factorial phosphate offset and the mean deep water phosphate content of the respective basin. Only in the two affected ocean basins (Indian Ocean 2000s vs 1990s and North Pacific 2010s vs 2000s), the absolute mean C* offset between the decades exceeds the standard deviation of the individual mean cruise offsets, indicating a robustness of the offset. Only in these basins and decades, we investigated the

crossover offsets of the three underlying variables DIC, TA and phosphate to determine data adjustments.

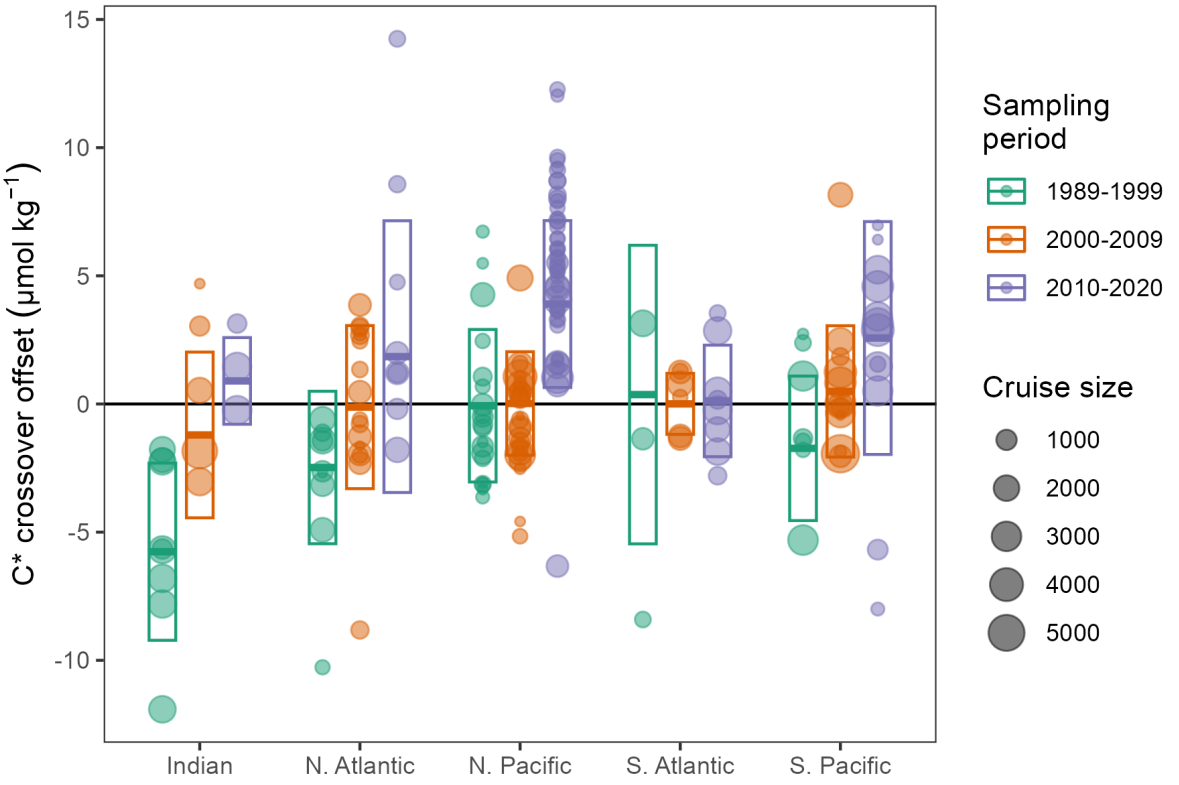

Fig. S3: Mean deep water cruise offsets in C* units against reference cruises from the 2000s. Colors distinguish cruises from each of our three sampling periods. Symbol size refers to the number of observations per cruise. The centre of the boxes indicate the mean offset across all cruises weighted by the number of observations per cruise, and the height represents the standard deviation across all offsets. The deep water crossover offsets shown here refer to the same depth thresholds also used by GLODAP to exclude data from the most variable parts of the ocean (Lauvset et al., 2021; Olsen et al., 2016), i.e. those sampled shallower than 1500 dbar in most regions.

Among the Indian Ocean data collected in the 1990s, more than 60% of the measurements were made in the framework of the WOCE sampling campaign with RV Knorr in 1994/95, identified as all Indian Ocean cruises with expocodes starting with 316N199. For these cruises, the offsets determined through the reanalysis of GLODAP crossover data are consistent in sign and magnitude with offset determined from measurements of certified reference materials for TA (Millero et al., 1998) and DIC (Johnson et al., 1998). In contrast to the general procedure applied to more recent cruises, the CRM offset determined for the RV Knorr cruises were not applied to the seawater measurements before the compilation of the data into GLODAP (Johnson et al., 2002).

According to the CRM measurement and in agreement with the mean decadal GLODAP crossover offset, we apply following bulk adjustments to all Indian Ocean RV Knorr cruises from the 1990s:

- TA: -3.5 µmol kg^{-1}
- DIC: +1.7 µmol kg^{-1}

The CRM based adjustments applied here were approved by the GLODAP reference group and applied in GLODAPv2.2022 (Lauvset et al., 2022).

According to the mean decadal GLODAP crossover offset, we further apply following bulk adjustments to all North Pacific cruises from the 2010s:

- TA: +2.05 µmol kg^{-1}
- DIC: -0.6 µmol kg^{-1}
- Phosphate: 1.007 (multiplicative adjustment)

It should be noted that our adjustments of the North Pacific data from the 2010s do not aim to improve the accuracy of these data, but to increase their consistency with the observations from the two previous sampling periods (1990s and 2000s), which were found to be internally more consistent (Fig. S3). Furthermore, all adjustments listed above are within the consistency targets and adjustments limits of GLODAP and would therefore not normally be adjusted during GLODAP's secondary quality control The offsets were only detected when analysing the crossover results from a decade-by-decade perspective as relevant to this study, and when converting the offsets from the individual parameters into C* units. It can thus not be concluded that the originally applied GLODAP adjustments are inappropriate.

In addition to the bulk adjustments listed above, we also tested a cruise-by-cruise adjustment of the data from the same periods, based on the mean offset of each cruise to cruises from the 2000s (Fig. S3). These tests revealed a largely consistent ΔC_{ant} reconstruction compared to the outcome with bulk adjustments (Fig. S9).

S1.3 Data gap-filling

The eMLR(C*) method requires that samples that are included in the analysis provide all required variables. Some cruises were initially not included after the flagging criteria were applied, because they lack measurements of only one of the nutrients (nitrate or phosphate) or TA for the calculation of C*. Our tests with synthetic data revealed that in some regions and decades the lack of the affected cruises is detrimental to the robustness of the ΔC_{ant} reconstructions, which was identified as an increase of the column inventory biases by more than a factor of two when comparing reconstructions with and without these data. The tropical Atlantic and the Southern Pacific were in particular affected by this lack of observations. To increase the robustness of our reconstructions through a better data coverage, we also include observations (Fig. 1 and Table S1) of nitrate, phosphate or TA that did not fulfil the strictest quality criteria (i.e. f-flag=2 and qc-flag=1). In cases where the flagging criteria were not met but data were provided through GLODAP, we used the available data. In cases where a parameter was not available at all, we used CANYON-B predictions (Bittig et al., 2018) for gap-filling, but only in cases where the required input parameters (including O_2) fulfilled our flagging criteria. The sufficient quality of all data sources used for the gap-filling (Table S1) was confirmed through additional quality assurance tests (see Table S1). The gap-filling procedure is reflected in our uncertainty assessment by including reconstructions with perturbed gap-filled data in our ensemble (Fig. S9).

Table S1: Gap-filling and quality assurance of observations that deviate from our standard flagging criteria (i.e., f-flag=2 and qc-flag=1), but were still included in the analysis to avoid large regional data gaps. Footnotes: (1)Wrongly assigned qc flags of 1 were identified in GLODAPv2.2021. This refers to DIC or TA data calculated from the fugacity of carbon dioxide (fCO_2). As fCO_2 was not secondary quality controlled, any derived parameter should carry a qc flag of 0, which was not always the case. This error was corrected for the purpose of this study and in GLODAPv2.2022 (Lauvset et al., 2022). (2)The offset of calculated TA data can plausibly be explained by any kind of TA contribution (e.g. from organic acids) that is not included in the acid-base system considered for the calculation. This "excess alkalinity" was previously estimated to be in the order of +4 µmol kg^{-1} in the open ocean (Fong and Dickson, 2019), which is in good agreement with the adjustment applied here.

Cruise expocodes	**Gap filling procedure**	**Quality assurance**
06MT19900123 316N19920502 316N19921006	Available TA data calculated from DIC and pCO_2 were used as provided by GLODAP.(1)	Additional GLODAP crossover with measured TA data from other cruises; Calculated TA data are on average 3 µmol kg^{-1} too low based on deep water crossover to directly measured TA, and were thus adjusted by this value(2)
31DS19940126	Measured nitrate data were used although GLODAP qc-flags do not meet our flagging criterion	As a sensitivity test we did run the eMLR method without nitrate as predictor variable (thereby including cruise 31DS19940126). The ΔC_{ant} reconstruction were found to be indistinguishable from those with the measured nitrate data
33MW19930704 33RO20030604 33RO20050111 33RO19980123	Missing phosphate data were filled with CANYON-B prediction	Additional GLODAP crossover with measured phosphate data from other cruises; Predicted phosphate data agree within ±1% to measured data for each of the four cruises
06AQ19980328	Missing TA data were filled with CANYON-B prediction	Additional GLODAP crossover with measured TA data from other cruises; The mean absolute crossover offset between the predicted and measured TA data is <0.5 µmol kg^{-1}

S2 Additional minor configuration changes of the eMLR(C*) method

In the following, we describe additional configuration changes of the eMLR(C*) method compared to the analysis by Gruber et al. (2019). These configuration changes were tested, but did not result in a relevant difference of the ΔC_{ant} reconstructions compared to our standard case and were thus not considered in our uncertainty budget (see supplement S4).

S2.1 Data thinning, subsetting and clustering

A random spatial subsampling procedure was introduced to thin the data from densely sampled regions, thus avoiding their disproportionate impact on the ΔC_{ant} reconstruction. The data thinning was achieved by grouping the observations within each neutral density slab on a 5°x5° horizontal grid. The total number of observations in each of the grid cells was counted. In the n-th quantile of grid cells with the highest number of observations, the observations were randomly subsetted to be identical to the highest number of observations within the remaining grid cells. This data thinning maintains the bulk of data and does not

increase the number of observations in poorly sampled regions, but it reduces the number of data points in highly sampled grid cells. It was found that up to a quantile threshold of n ≈ 0.3, the data thinning has no noticeable effect on the ΔC_{ant} reconstructions, indicating a robustness of the eMLR(C*) results to uneven sampling distribution. A moderate thinning with n = 0.05 was used for our analysis.

A bottom depth threshold of 500m was tested to exclude observations from continental shelves. The ΔC_{ant} reconstructions with and without the observations from the coastal shelf were very similar. The removal of shelf data was thus not further considered.

For our standard configuration of the eMLR(C*) method, the data were clustered vertically into the neutral density slabs previously defined by Gruber et al. (2019), i.e., slabs with boundaries at 26.00, 26.50, 26.75, 27.00, 27.25, 27.50, 27.75, 27.85, 27.95, 28.05, 28.10, 28.15, 28.20 kg m^{-3}, of which the two highest density boundaries were only used in the Atlantic Ocean. Neutral densities were calculated from salinity and temperature following Jackett and McDougall (1997). Halving the number of these density slabs by combining two adjacent slabs did not strongly impact the outcome. The general spatial ΔC_{ant} distribution was even maintained when no slab separation was applied. We thus deem the slab separation to be of secondary importance for our analysis and included only reconstruction based on the standard density slabs in our uncertainty assessment.

S2.2 MLR model selection criteria

Among the 2 x 120 MLR models fitted for each density slab and decade, the best models were selected. As a first step, MLR models with a combination of multicollinear predictors were removed. These models were identified as those with a variance inflation factor (VIF) higher than 500, which is an alternative procedure to the previous arbitrary decision to limit the maximum number of predictors to 5 out of 7 (Gruber et al., 2019). The selected VIF of 500 represents a rather weak threshold, as our test with synthetic data revealed that stricter removal criterion (e.g. VIF ≤ 100) increases the biases of the ΔC_{ant} column inventories. The rather weak sensitivity of the eMLR outcome to the VIF threshold indicates a general robustness of the eMLR(C*) method to multicollinearity of predictors.

Among the remaining MLR models, the 10 models with the lowest summed root mean squared error (RMSE) across both sampling periods were selected for the ΔC_{ant} prediction. The Akaike information criterion (AIC) was tested as an alternative model selection criteria to the RMSE. Both approaches result in essentially identical ΔC_{ant} reconstructions, indicating a robustness of the eMLR(C*) method toward overfitting the data.

We did perform ΔC_{ant} reconstructions after individually removing each of the predictor variables. It was found that any predictor can be removed without a noticeable impact on the ΔC_{ant} reconstruction, with the exception of the nutrient that was used for C* calculation. This indicates a certain redundancy among the complete set of possible predictor variables, which is consistent with the finding that the avoidance of predictor collinearity based on the VIF criterion has only a weak impact on the ΔC_{ant} reconstruction.

S3 Additional observation-based results

S3.1 Column inventory maps of β

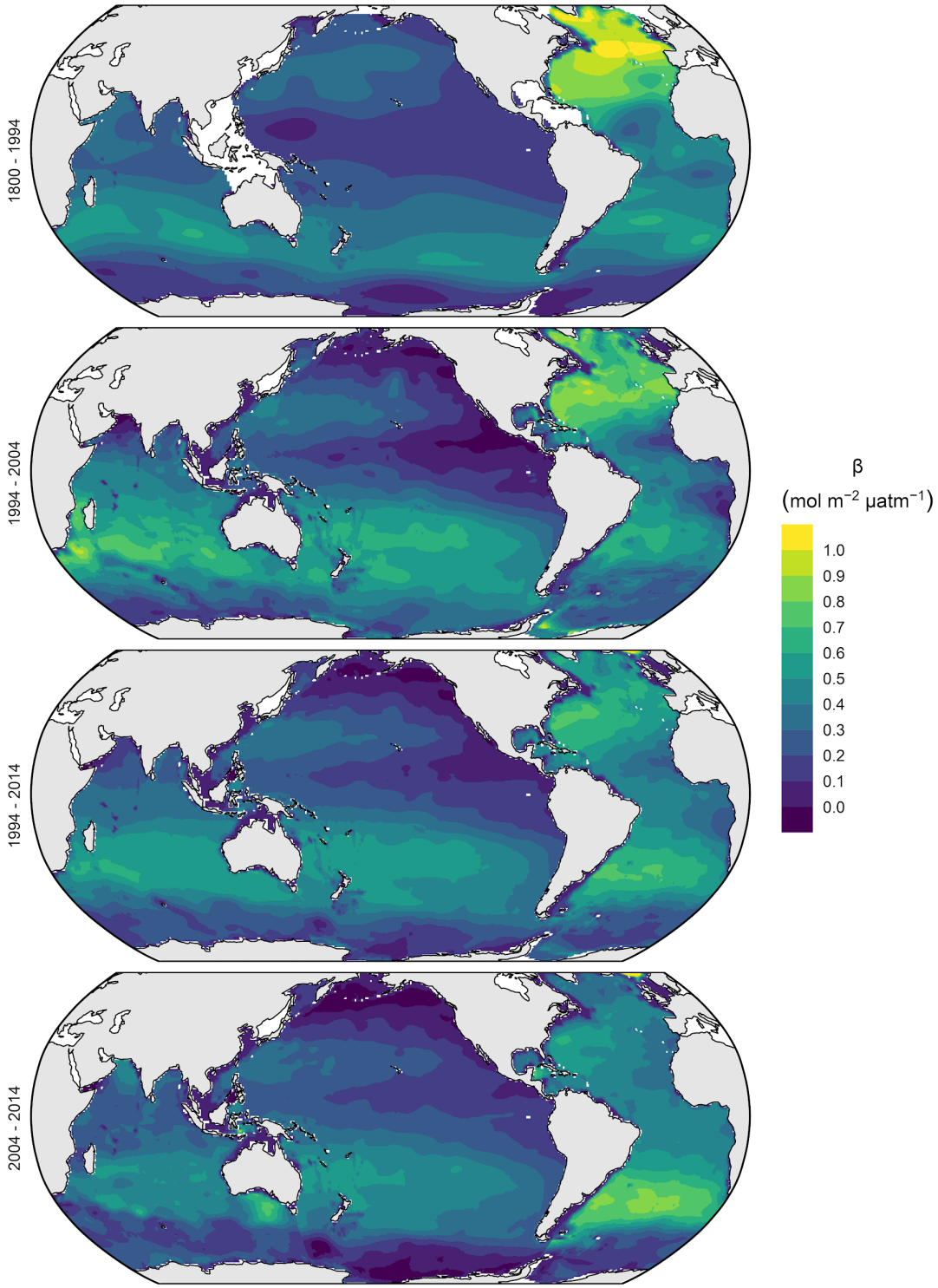

Fig. S4: Column inventory maps of β = ΔC_{ant} / $\Delta pCO_{2,atm}$ for the preindustrial period from 1800–1994, as well as for the two decades and the 20-year period analysed in this study.

S3.2 Regional and global mean β column inventories

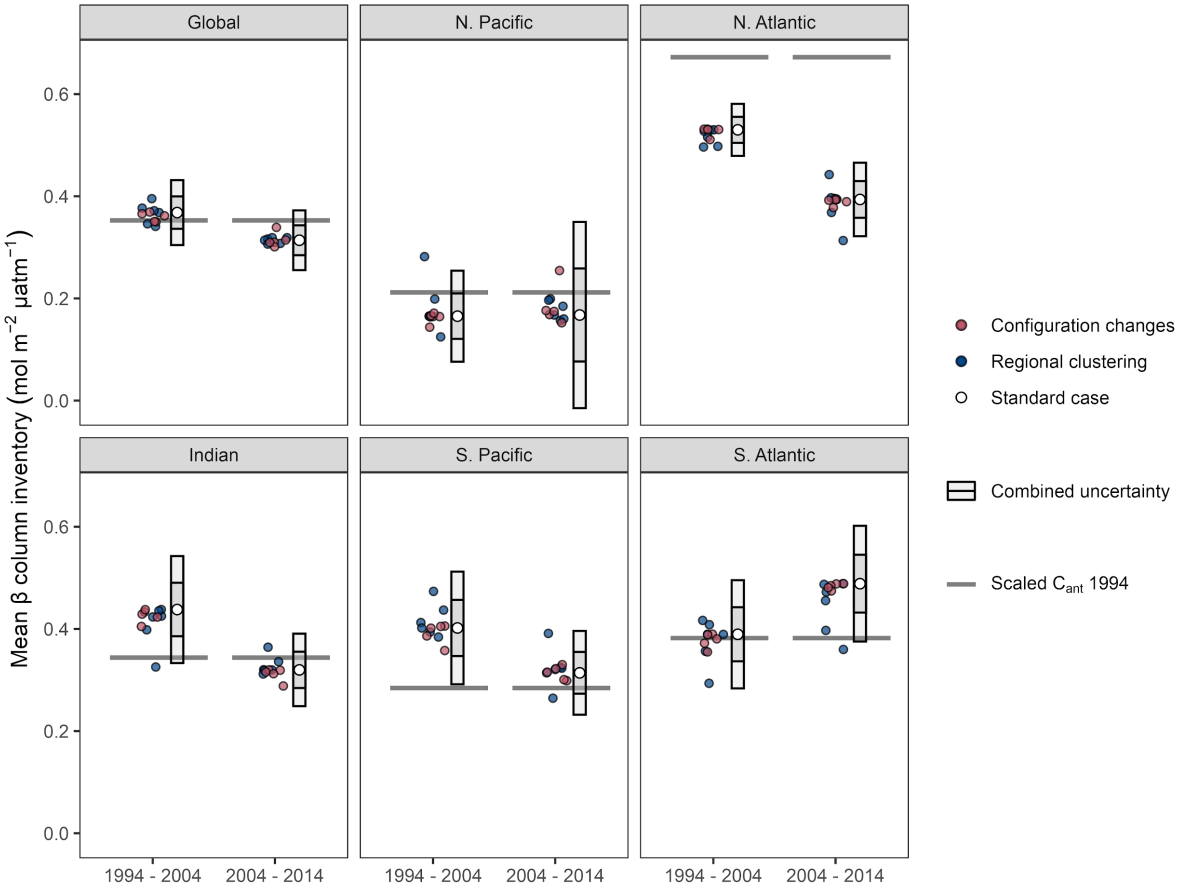

Fig. S5: Global and regional mean column inventories of $\beta = \Delta C_{ant} / \Delta pCO_{2,atm}$ for the decades 1994–2004 and 2004–2014. White points represent the standard case and error bars the 1σ- and 2σ-uncertainty ranges. Other points represent ΔC_{ant} reconstructions considered for the uncertainty assessment (red: configuration changes; blue: regional clustering). Horizontal lines indicate β inventories based on the total C_{ant} storage in 1994 (Sabine et al., 2004).

S3.4 Reproduction of the study by Gruber et al. (2019)

In addition to our estimates for the two decades since 1994, we reconstructed ΔC_{ant} from 1994–2007 to test the consistency of our approach with the analysis by Gruber et al. (2019). For this purpose, we clustered the observations into the same sampling periods (1982–1999 and 2000–2014) used by Gruber et al. (2019), while maintaining all other configurations of the eMLR(C*) method as applied in this study. With this approach, we find indistinguishable global ΔC_{ant} inventories (33 ± 4 Pg C vs 34 ± 4 Pg C) and very similar spatial distribution of the column inventory changes from 1994–2007 (Fig. S6). This agreement underlines the robustness of our findings and similarity of the approaches when taking into account that we used different releases (v2 vs v2.2021) of GLODAP (Lauvset et al., 2021; Olsen et al., 2016) and the World Ocean Atlas (Locarnini et al., 2019; Zweng et al., 2019), introduced modification of the eMLR(C*) method and applied data adjustments. It should be noted that the analysis of Gruber et al. (2019) is based on unadjusted Indian Ocean data from the 1990s, but in their standard case, which combines the Indian Ocean and Pacific into one

spatial cluster (basin mask “2” in Fig. S1), the regional impact of the unadjusted data is less pronounced compared to a separate analysis of the Indian Ocean as performed in this study and the sensitivity cases 107 and 110 of Gruber et al. (2019). The less pronounced impact of the unadjusted data in the Indian Ocean in the earlier study could also partly be due to the manual removal of “stations with an excessive amount of scatter in the computed C* tracer” (Gruber et al., 2019).

The analysis for the 1994–2007 periods incorporates observations from 2000–2014 for the second sampling period, i.e., only data collected since 2015 are used for the first time in our analysis of the 2004–2014 decade. The fact that the increasing C_{ant} storage rates in the South Atlantic Ocean emerge already in the 1994–2007 reconstruction, while the North Atlantic Ocean still maintains a relatively strong, yet already weaking storage rate, is most likely due to the incorporation of a good fraction of the observations from the early 2010s in the analysis of the 1994–2007 period.

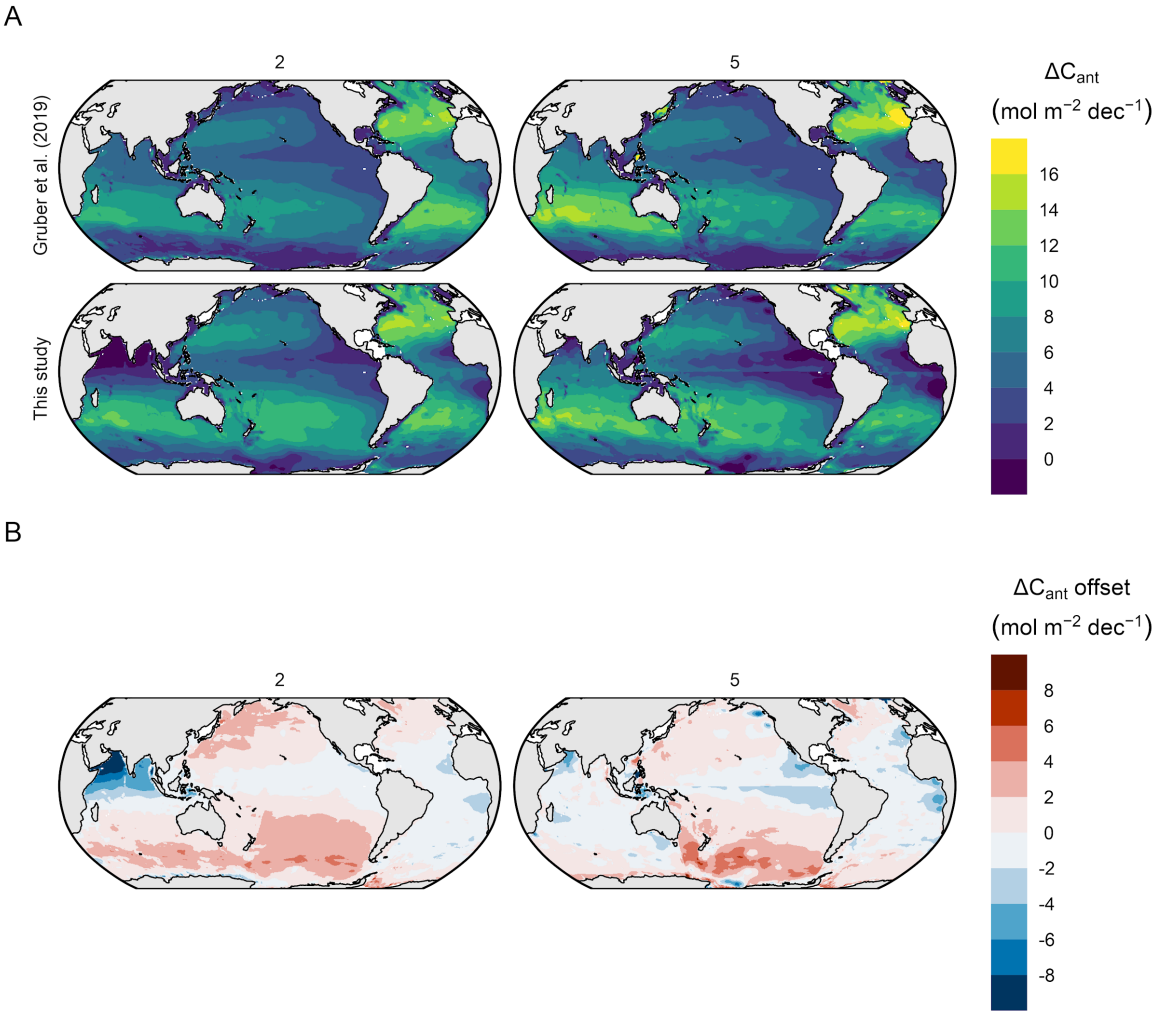

Fig. S6: Column inventory maps of (A) ΔC_{ant} for the period 1994-2007 as analysed by Gruber et al. (2019) and in this study (panel rows). Reconstructions are shown for the two regional clustering schemes “2” and “5” (Fig. S1) that were applied in both studies (panel columns). (B) ΔC_{ant} offset between Gruber et al. (2019) and this study.

S3.5 Zonal mean sections of ΔC_{ant}

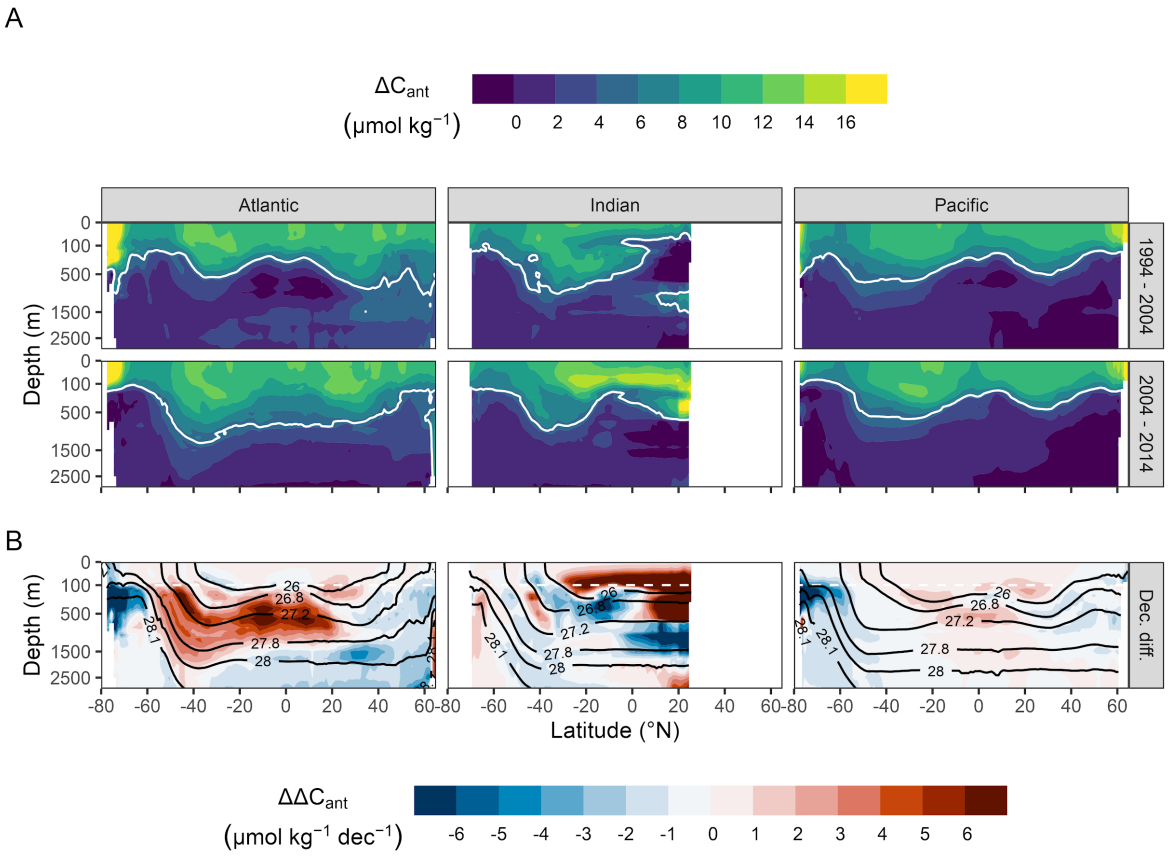

Fig. S7: Zonal mean sections of (A) ΔC_{ant} for each ocean basin (columns) and decade (rows). White contour lines highlight a ΔC_{ant} level of 5 μmol kg^{-1} dec^{-1}. (B) Decadal differences in the storage changes ($\Delta\Delta C_{ant}$). Black contour lines indicate isoneutral density levels, where the selected boundaries represent every second density slab used to cluster the data in the vertical dimension.

The strong decadal differences between the ΔC_{ant} zonal mean sections in the Northern Hemisphere of the Indian Ocean (Fig. S7B) are a consequence of the lack of observations in the Arabian Sea during the central sampling period (2000–2009) of our analysis. This data sparsity requires strong spatial extrapolation to reconstruct the C* distribution, which leads to higher uncertainties. The resulting bias structures according to our tests with synthetic data (Fig. S16) are almost mirrored in the Northern Hemisphere of the Indian Ocean for the 1994–2004 and 2004–2014 decade, because the data sparsity in the central sampling period affects both reconstructions inversely. In terms of the ΔC_{ant} column inventories, the positive (surface) and negative (1000–1500 m) extrapolation errors in the Northern Indian Ocean largely cancel out (Fig. S13). In terms of the mean ΔC_{ant} profiles (Fig. 4A) and whole-basin inventories (Figs. 4B and 5) for the Indian Ocean, the impact of the extrapolation uncertainty is negligible due to low volume of the affected water masses. Our 20yr reconstruction from 1994–2014 is also not affected by this issue, because it does not require data from the central sampling period (2000–2009).

S3.6 Residuals of MLR models

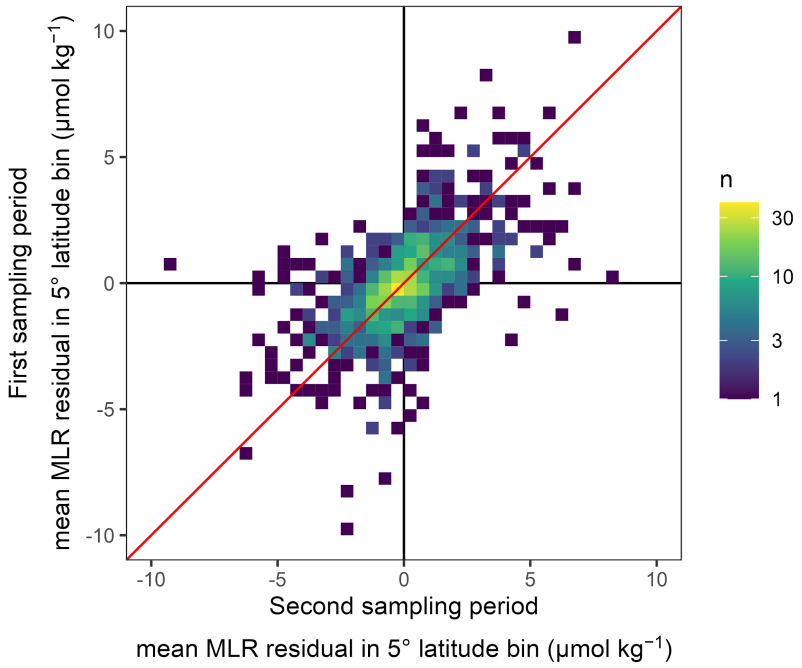

Fig. S8: Residuals of the MLR models averaged over 5° latitude bins within each density slab, shown as a heatmap of residuals from the first in comparison to the second sampling period. The correlation coefficient is 0.56.

S4 Determination of uncertainty based on configuration changes of the eMLR(C*) method

S4.1 Uncertainty quantification

Our primary uncertainty quantification is based on an ensemble of ΔC_{ant} reconstructions that differ with respect to the specific configuration of the eMLR(C*) method. For this purpose, we identified the most impactful configuration changes of the method that are still believed to provide an equally likely representation of the true ΔC_{ant} distribution as our standard case. The following description of our uncertainty quantification refers to the ΔC_{ant} reconstructions as the primary outcome of our analysis, but applies analogously to other derived estimates such as the mean penetration depth of ΔC_{ant}, β, or the ocean-borne fraction of CO_2 emissions.

One of the most important configuration choices of the eMLR(C*) method is the regional clustering of the data for the MLR fitting and mapping of ΔC_{ant}. In total, we applied six different basin mask definitions (Fig. S1), of which the basin mask "3" is used for our standard case reconstruction. The mean absolute difference (s_{reg}) between the ΔC_{ant} reconstructions obtained with basin mask "3" and the five alternative basin masks is considered as one component of our uncertainty budget.

The other configuration changes considered in our uncertainty estimate are:

1. Cruise-by-cruise data adjustments: Individual cruise adjustment values according to our crossover analysis (Fig. S3) were applied instead of a bulk adjustments (see supplement S1.2)
2. Modified gap-filling: Perturbations were applied to the gap-filled data reflecting the crossover offset between the gap-filled data and observations available from GLODAPv2.2021. Specifically, we perturbed CANYON-B predictions for TA with an offset of 1 µmol kg^{-1} and for phosphate data with a factorial offset of 1.01. Calculated TA data were perturbed with an offset of 3 µmol kg^{-1} (see supplement A1.3).
3. C*(N,TA) as target variable: Nitrate and TA rather than phosphate and TA were used for the calculation of C*.
4. Surface ΔC_{ant}: The surface ocean ΔC_{ant} was not estimated with the atmospheric equilibrium approach, but based on the observation-based surface ocean DIC product OceanSODA (Gregor and Gruber, 2021). To eliminate local and short-term variability in DIC from this product, a local linear regression for DIC as function of $pCO_{2,atm}$ was fitted for the period 1990–2020. Based on the slope of this regression, the surface ocean DIC increase was predicted between the reference years 1994, 2004 and 2014 according to the increase in $pCO_{2,atm}$.
5. WOA18 predictors: Nutrients and oxygen from World Ocean Atlas 2018 (Locarnini et al., 2019; Zweng et al., 2019) were used for the mapping of ΔC_{ant}, instead of the gridded climatologies based on GLODAPv2 (Lauvset et al., 2016).

For each of these five additional configuration choices, we calculated the difference between the ΔC_{ant} reconstructions obtained with standard configuration and the modified configuration ($s_{config,1\text{-}5}$), all of which were obtained using the basin mask "3".

For our global ΔC_{ant} inventories we consider an additional uncertainty component ($s_{scaling}$) arising from the upscaling of the directly mapped ΔC_{ant} inventories by +7% to account for storage changes in unmapped regions and the deep ocean. The uncertainty contribution is assumed to be half of the absolute scaling value, i.e. ±3.5% of the global ΔC_{ant} inventories. This assigned scaling uncertainty reflects the uncertainty in the underlying regional inventories and the potential for their non-steady growth.

The combined uncertainty was determined as the square root of the sum of squares (RSS) of the individual uncertainty components:

$$s_{combined} = \sqrt{s_{reg}^2 + \sum_{i=1}^{5} s_{config,i}^2 + s_{scaling}^2}$$

We consider the combined uncertainty $s_{combined}$ as standard uncertainty ($\pm 1\sigma$) of our reconstructions representing a 68% confidence interval. We derive the expanded uncertainty of our estimates through multiplication of $s_{combined}$ with a factor of 2. The obtained expanded uncertainty ($\pm 2\sigma$) represents a confidence interval of 95%. All results are reported with $\pm 1\sigma$ uncertainty ranges. A difference between two estimates is considered significant if the absolute difference is larger than the combined uncertainty, i.e., the RSS of the 1σ-uncertainties of both estimates.

The individual uncertainty components s_{reg} and $s_{config,1\text{-}5}$ are displayed at the 1σ-level for column inventories in Fig. S9 and for inventories in Fig. 6. Fig. 6 also includes $s_{scaling}$ for the global estimate. The combined uncertainty $s_{combined}$ at the $\pm 1\sigma$ level is displayed for column inventories in Fig. S10.

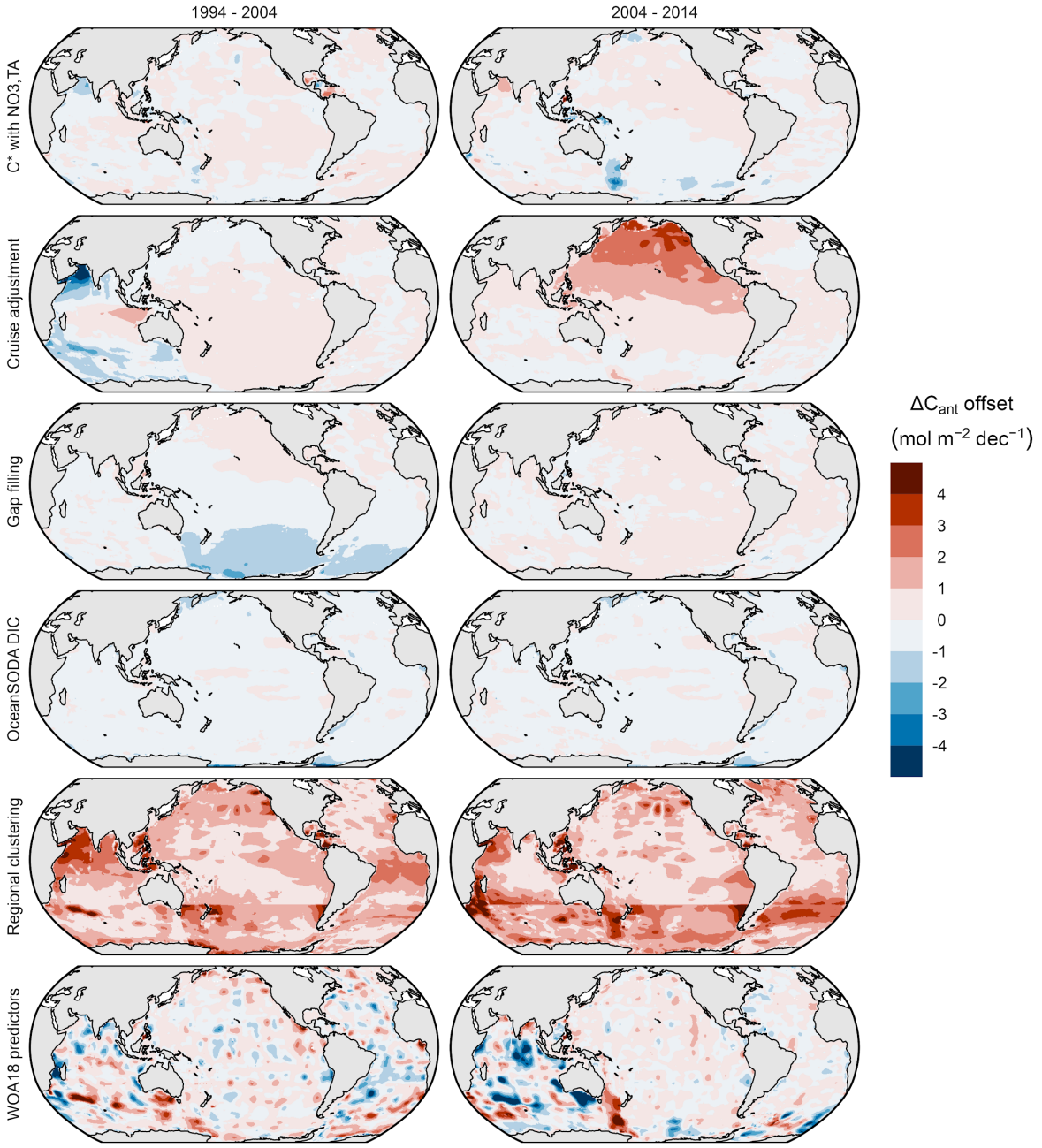

Fig. S9: Individual column inventory uncertainty contributions determined as offsets between our standard case reconstruction and six configuration choices of the eMLR(C*) method (panel rows) for both decades (panel columns). Negative values indicate that lower column inventories were obtained with the configuration changes. The regional clustering offsets are positive by definition, as they represent the mean absolute offsets across five alternative basin masks.

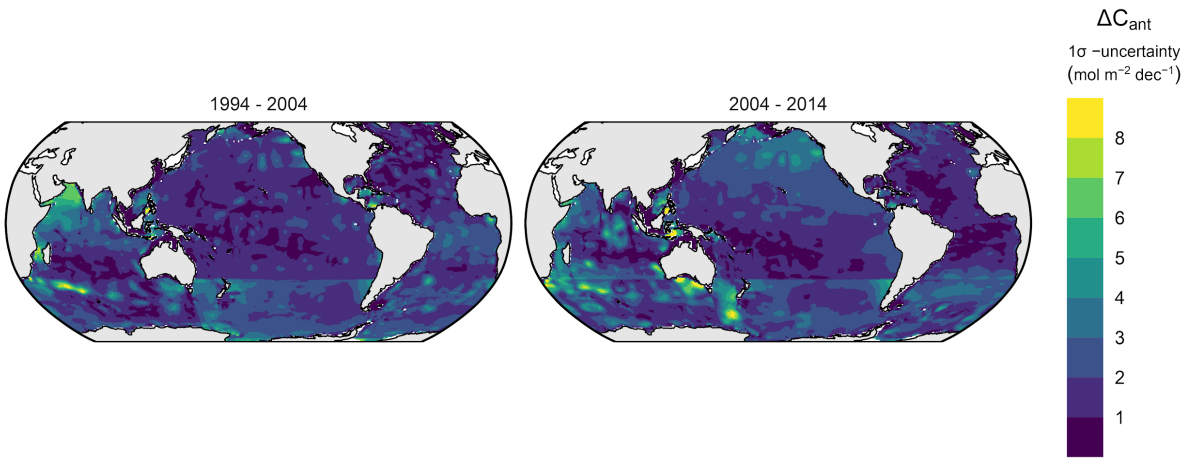

Fig. S10: Combined column inventory uncertainties at the 1σ-uncertainty level. Panel rows distinguish the two reconstructed decades. The combined uncertainties are determined as the square root of summed squared offsets (RSS) of the individual uncertainty components shown for observations in Fig. S9.

S4.2 Further sensitivity analysis

Following the same approach as for the primary uncertainty quantification described above (supplement S4.1), we assess the sensitivity of our ΔC_{ant} reconstructions to additional configuration choices of the eMLR(C*) method. These reconstructions are not believed to provide an equally likely representation of the true ΔC_{ant} distribution as our standard case, but are intended to illustrate the sensitivity to certain aspects of the method such as the data coverage or data consistency. The considered changes of the configuration are:

1. No data adjustment: All data are used as published in GLODAPv2.2021 (see supplement A1.2).
2. Reoccupation filter: Only data from sections that were reoccupied are used. The filtering criterions is that at least one record must be available within a density slab and 1°x1° horizontal grid box for each of two compared sampling periods.
3. C*(P) target variable: C* was calculated only with phosphate (neglecting TA).
4. DIC target variable: DIC was used as a target variable, i.e. without removing a nutrient or TA contribution and without adjusting to the reference year (t_{ref}).
5. No tref adjustment: Calculation of C* based on phosphate and TA as in the standard case, but without temporal adjustment to the reference year (t_{ref}).

The individual sensitivity components are displayed at the 1σ-level for column inventories in Fig. S11 and for inventories in Fig. S12.

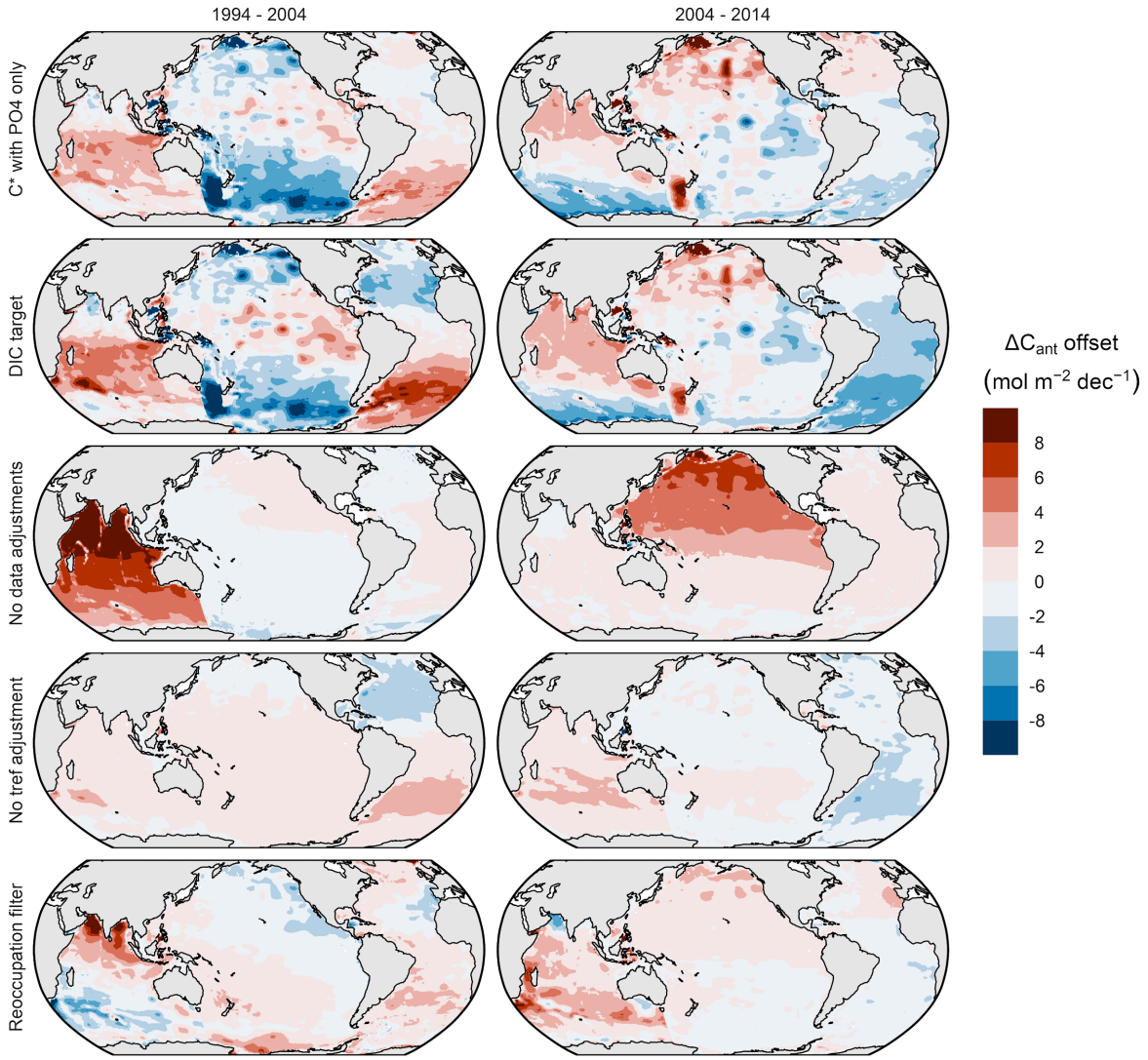

Fig. S11: Column inventory sensitivity to specific aspects of the eMLR(C*) method at the 1σ-uncertainty level determined as offsets between our standard case reconstruction and five sensitivity reconstructions (panel rows) shown for both decades (panel columns). Negative values indicate that lower column inventories were obtained with the sensitivity tests. Note that the sensitivity reconstructions are not included in the uncertainty budget as they are not considered an equally likely representation of the true ΔC_{ant} signal.

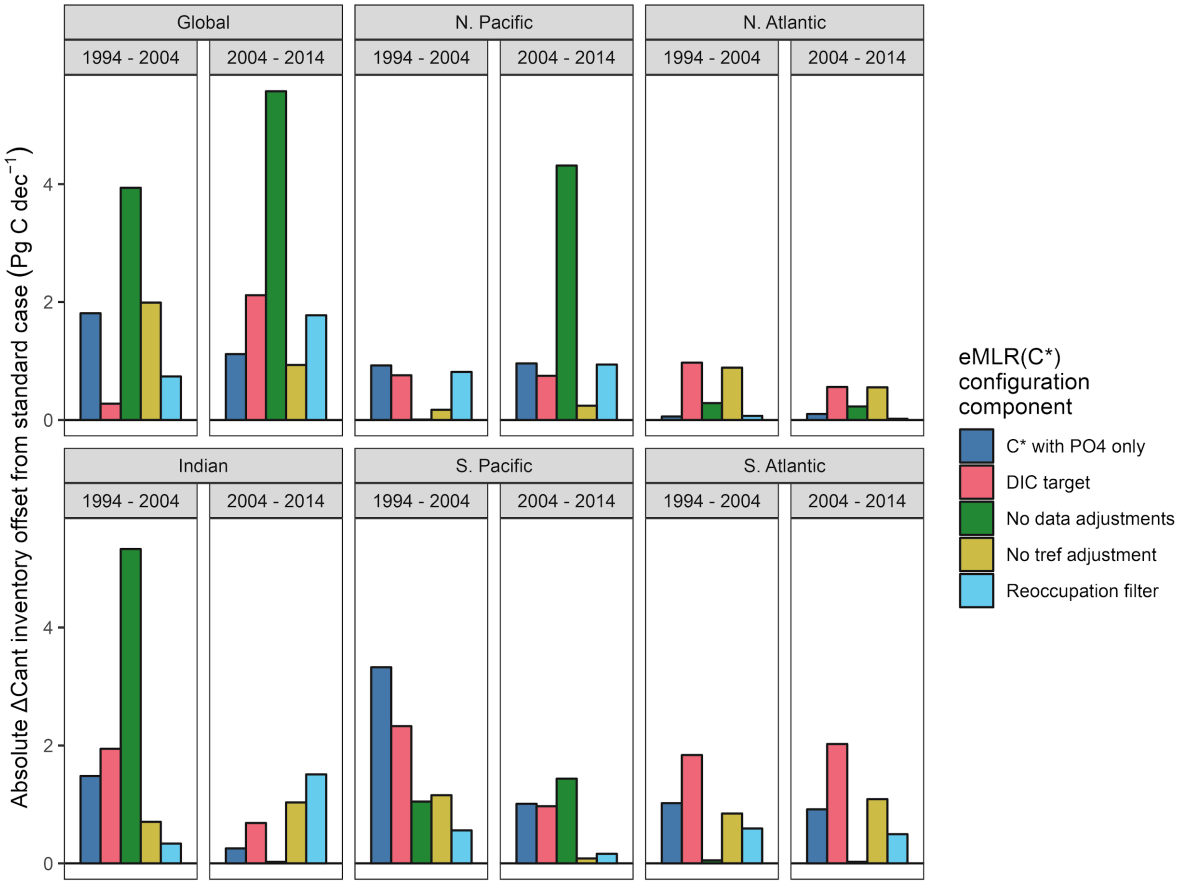

Fig. S12: Inventory sensitivity at the 1σ-uncertainty level determined as offsets between our standard case reconstruction and five sensitivity configurations of the eMLR(C*) method (colours) for each ocean region and both decades (panels). All offsets are shown as absolute values. Note that the sensitivity reconstructions are not included in the uncertainty budget as they are not considered an equally likely representation of the true ΔC_{ant} signal.

S5 Testing of the eMLR(C*) method with synthetic data

For the purpose of testing the eMLR(C*) method with respect to biases that cannot be retrieved from its application to observational data, we generated a synthetic data set which contains data that were subsetted from a GOBM according to the spatio-temporal coverage of real-world observations available through GLODAP. Applying the eMLR(C*) method to this synthetic data set allows us to compare the reconstructed ΔC_{ant} distribution to the model truth and thereby assess the quality of the reconstruction. The assessment with synthetic data was previously used for the development of the eMLR(C*) method and was described in detail by Clement and Gruber (2018).

S5.1 Generation of synthetic data from CESM model

The synthetic data set used in this study was generated from the Community Earth System Model (CESM), an ocean circulation hindcast model with embedded biogeochemistry (Doney et al., 2009). After a 180-year spin-up phase, two model runs A and D were split up and forced with the historic (Dlugokencky and Tans, 2019) and preindustrial atmospheric CO_2 concentration, respectively. Both runs were forced with historic surface-atmospheric data from JRA55-do (Tsujino et al., 2018) during the analysis period. The raw model output was horizontally regridded to a regular 1°x1° grid, while the original irregular 60 depth levels were maintained. The model output used in this study was also submitted and analysed in phase 2 of the REgional Carbon Cycle Assessment and Processes project (RECCAP2) and will be made available upon completion of this project (Poulter et al., 2022).

The synthetic data set was created by subsetting model run A (increasing atmospheric CO_2, variable climate). Therefore, the model output was linearly interpolated between depth levels to match the exact sampling depth in GLODAP. Annually averaged model truth fields of total C_{ant} were calculated as the difference in DIC between model runs A and D (preindustrial atmospheric CO_2, variable climate). ΔC_{ant} was calculated as the difference between total C_{ant} at the second (t_{ref2}) and first (t_{ref1}) reference year of each analysis decade. Climatological fields of the predictor variables were calculated as the annual average of the year 2007.

S5.2 Method evaluation results

Our tests with synthetic generated from the GOBM confirm that the eMLR(C*) method is capable of retrieving the global ΔC_{ant} patterns in the horizontal (Fig. S13) and vertical (Figs. S16 and S17A) dimension when applied to data that represent the spatio-temporal coverage of observations available for the past three decades. The absolute column inventory biases of our standard case reconstruction (Fig. S13B) are below 2 mol m^{-2} dec^{-1} for most parts of the ocean (87% of the total surface area), and only in a few regions increase up to 4 mol m^{-2} dec^{-1} (13%) or exceed the latter threshold (<0.5%). In contrast, the ΔC_{ant} column inventories in our model are larger than these thresholds of 2 and 4 mol m^{-2} dec^{-1} over more than 55 and 90% of the surface area of the ocean, respectively (Fig. S13A). Likewise, the biases of the standard case reconstruction in the zonal mean sections (Fig. S16B) are mostly within 2 µmol kg^{-1}, which is about half as much as the decadal changes in the observation-based ΔC_{ant} reconstructions (Figs. 3 and S7).

When comparing the ΔC_{ant} depth layer inventories of our standard case reconstructions to the model truth (Fig. S17B), we find that in most ocean basins and depth layers the offsets

are within the 2σ-uncertainty range determined from our ensemble of eMLR(C*) reconstructions. When comparing the reconstructed ΔC_{ant} inventories integrated over the top 3000 m to the model truth (Fig. S18), we find that out of the 12 reconstructed ΔC_{ant} inventories, 7 and 11 revealed a bias that is within the 1σ- and 2σ-uncertainty range (Fig. S18), which meets the expectation of 68% and 95% confidence intervals, respectively. Only the bias of our standard case inventory for the South Atlantic slightly exceeds the 2σ-uncertainty range for the 2004–2014 decade.

When interpreting the outcome of our tests with synthetic data, it should be taken into account that the CESM model that we used as a testbed reveals a lower decadal ΔC_{ant} variability than our observation-based reconstructions, as well as a generally low C_{ant} storage in the North Atlantic due to a weak AMOC in the model. It should further be noted that any potential model drift would affect the synthetic data generated from run A, but not the model truth ΔC_{ant} field which is calculated as a difference of two model runs (A and D). Thus, our bias estimate also includes a model drift component.

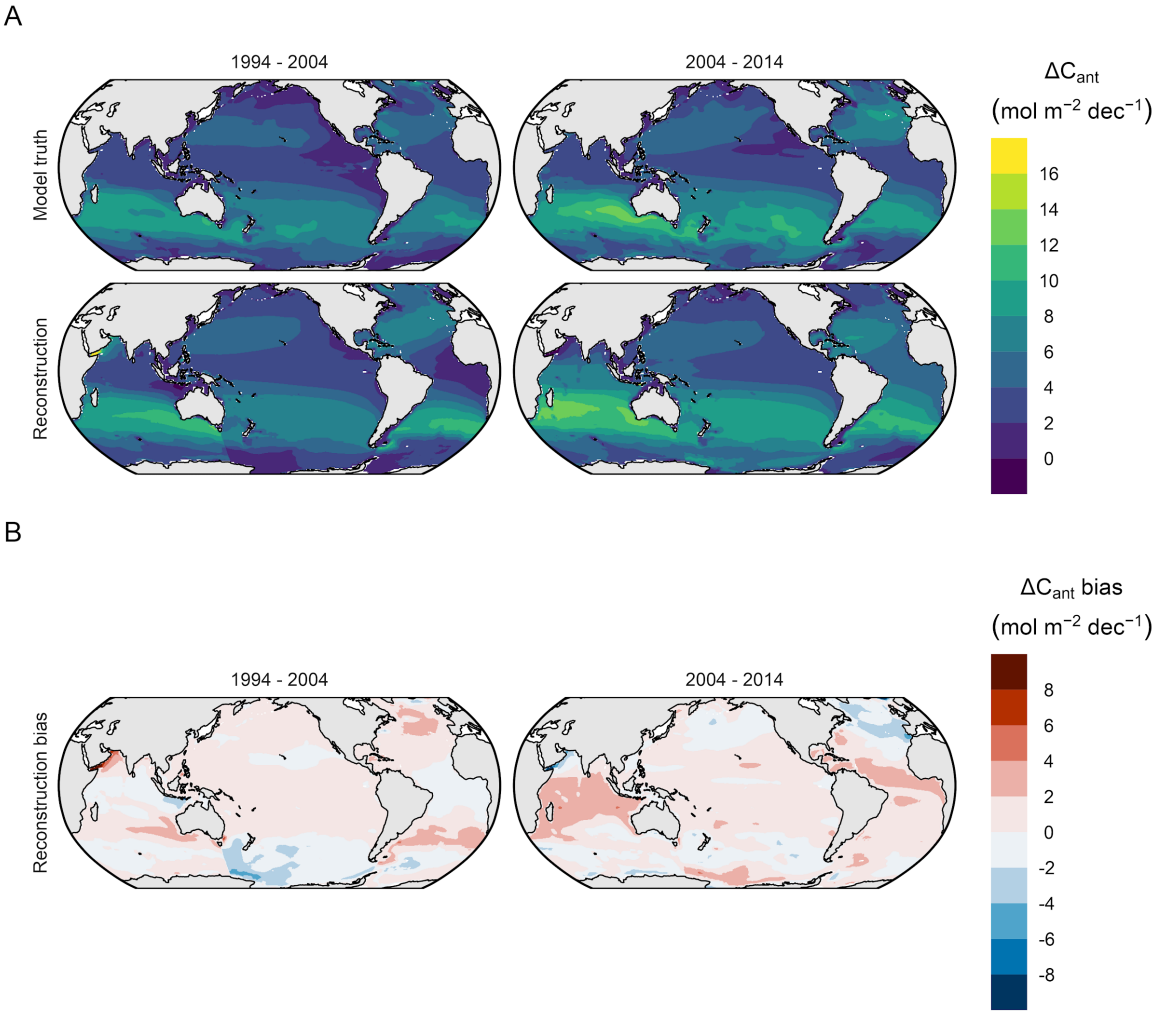

Fig. S13: Column inventory maps of changes in anthropogenic CO_2 (ΔC_{ant}) integrated over the upper 3000m, comparing the eMLR(C*)-based reconstructions with the model truth. (A) Absolute ΔC_{ant} for two decades from 1994 to 2014. (B) Bias in the eMLR(C*)-based reconstructions compared to the model truth as shown in (A).

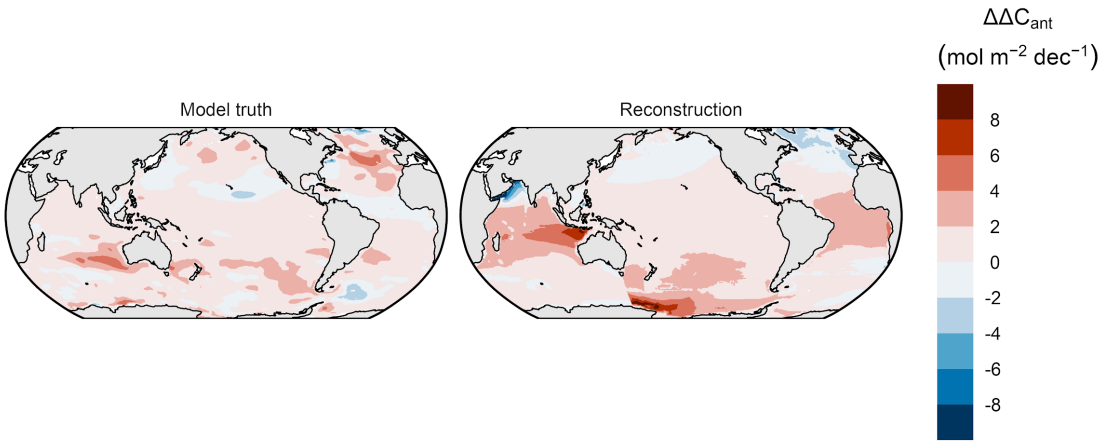

Fig. S14: Same as Fig. S13B, but contrasting the reconstructed decadal differences ($\Delta\Delta C_{ant}$) in the storage changes with the model truth, instead of showing the reconstruction bias for both decades.

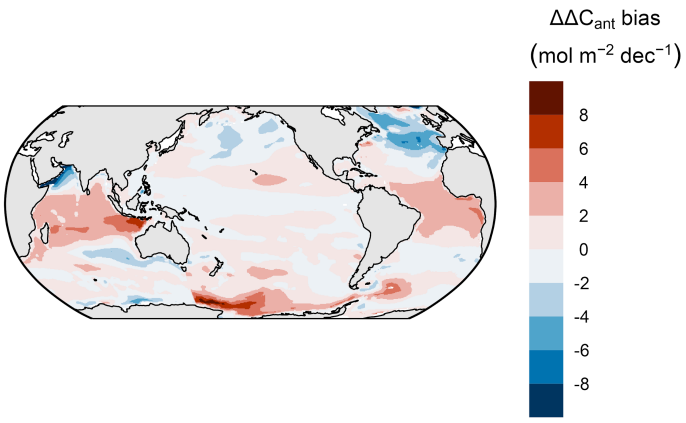

Fig. S15: Same data as Fig. S14 but showing the bias in the decadal differences ($\Delta\Delta C_{ant}$ bias) in the storage changes by subtracting the model truth from the reconstruction.

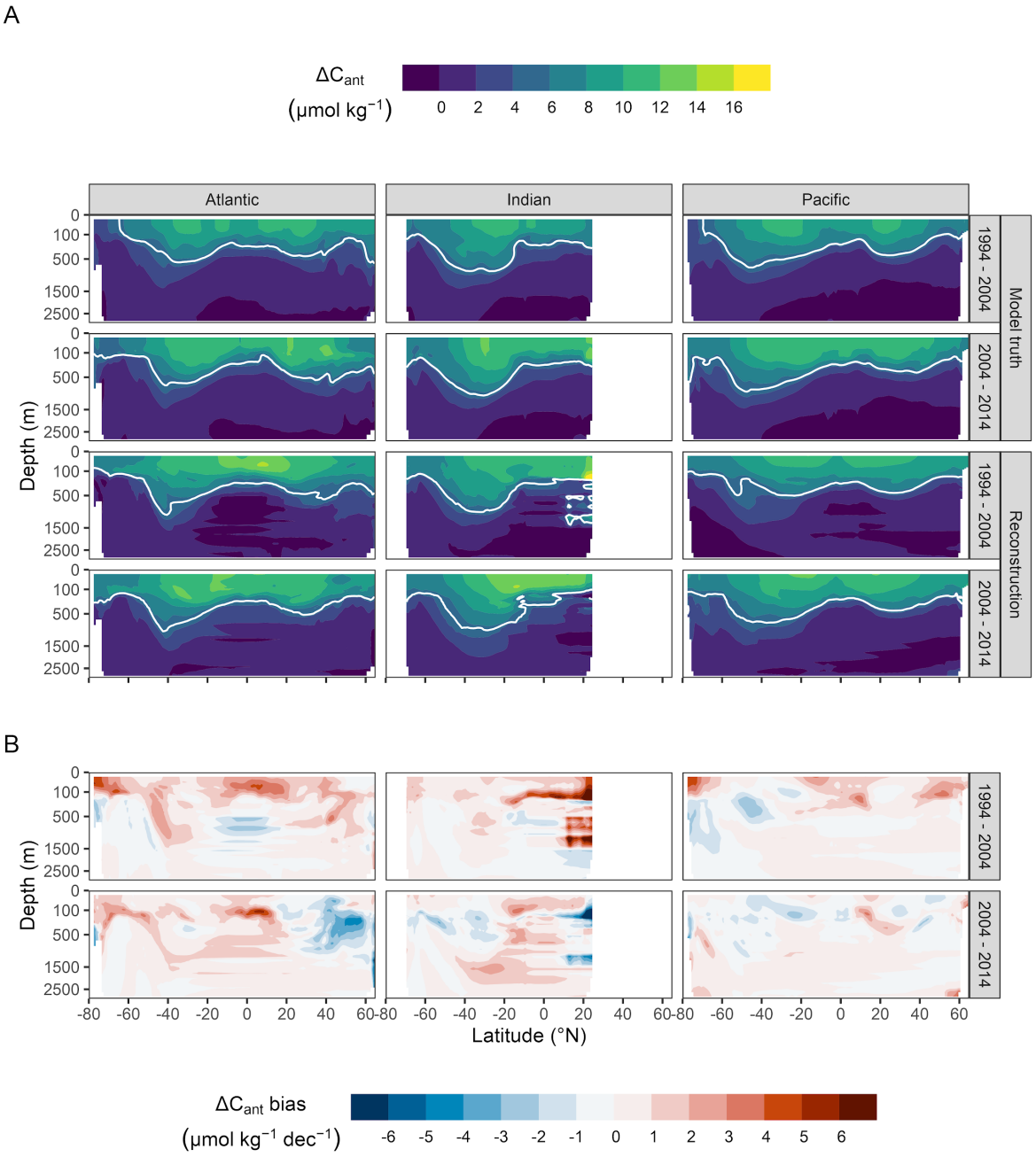

Fig. S16: Zonal mean sections of (A) ΔC_{ant} for each ocean basin (columns) and two decades (rows), comparing the eMLR(C*)-based reconstructions with the model truth. White contour lines indicate a ΔC_{ant} leval of 5 μmol kg^{-1} per decade. (B) Bias in the eMLR(C*)-based reconstructions compared to the model truth as shown in (A).

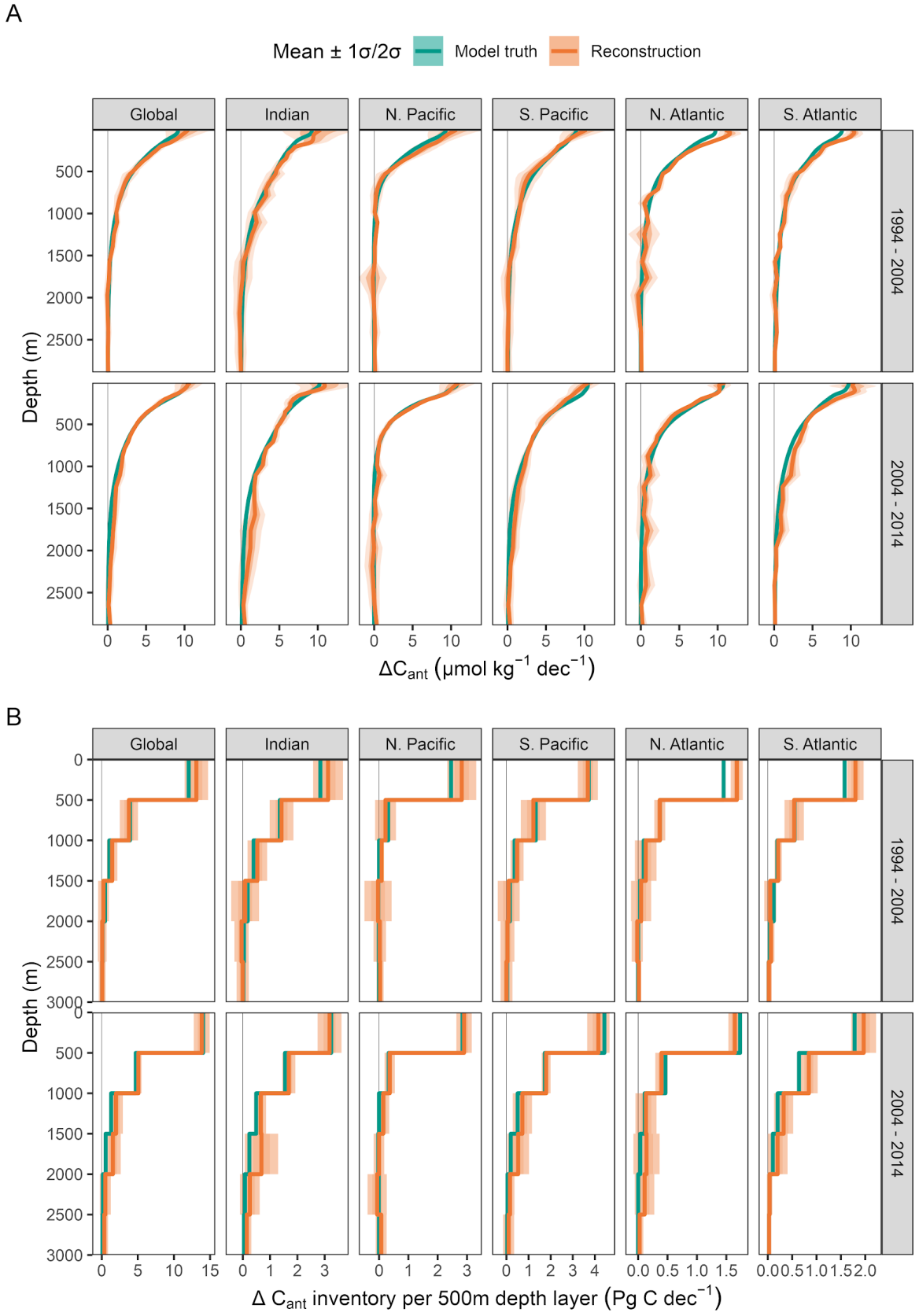

Fig. S17: (A) Mean profiles and (B) 500m depth layer inventories of the changes in anthropogenic carbon content (ΔC_{ant}) for each hemispheric basin and the global ocean (columns) as well as the two decades since 1994 (rows). Colours distinguish the eMLR(C*)-based reconstructions and the model

truth. Thick lines represent the standard case reconstruction and the model truth of ΔC_{ant}, while ribbons indicate the 1σ- and 2σ-uncertainty ranges of the reconstructions based on an ensemble of reconstructions. Note that the model truth estimates do not have an uncertainty ribbon.

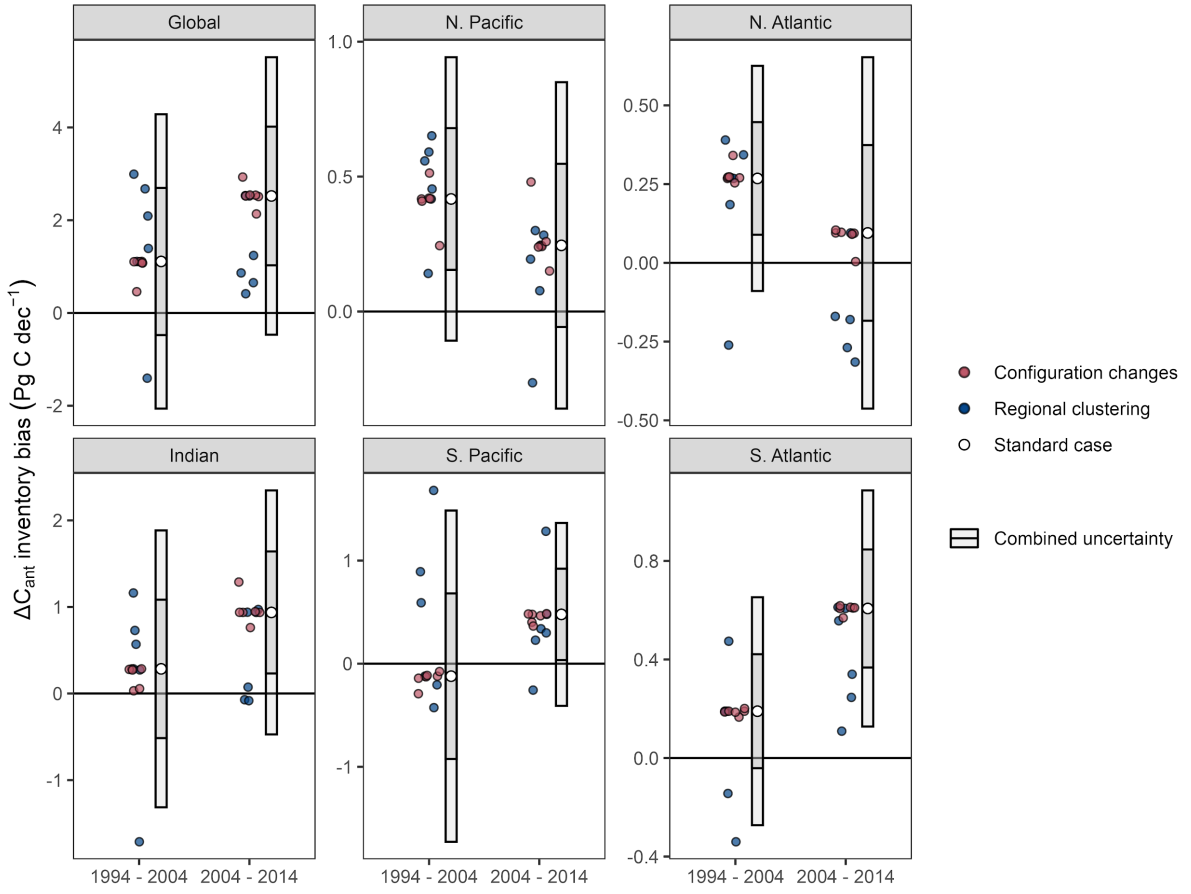

Fig. S18: Biases in the ΔC_{ant} inventories for each ocean basin and the global ocean, and the decades 1994–2004 and 2004–2014. White symbols represent the standard case of our ΔC_{ant} reconstructions and error bars the 1σ- and 2σ-uncertainty ranges. Coloured points represent ΔC_{ant} reconstructions considered in the uncertainty assessment (red: configuration changes of the eMLR(C*) method; blue: regional clustering).

S6 Comparison of regional ΔC_{ant} inventories to previous studies

In the following, we provide a detailed comparison of our ΔC_{ant} inventories for each hemisphere of the main ocean basins (Table 1) to previous regional estimates. The selected regional studies rely — like our reconstructions — on ocean interior biogeochemical observations, apply an MLR approach, and cover multiple time periods. All regional analyses compare individual reoccupied sections as a first step and subsequently extrapolate the ΔC_{ant} reconstruction from a single or multiple sections to the whole basin. This stands in contrast to our global eMLR(C*) approach, which uses all observations from one spatial cluster together in a single MLR fitting procedure. In general, it can thus be assumed that the global eMLR(C*) approach is less sensitive to measurement biases of individual cruises but also less sensitive to small scale ΔC_{ant} signals (Carter et al., 2019). For consistency with our reporting, we converted the uncertainty estimates of the regional studies to 1σ uncertainty ranges whenever possible, while potential differences in the exact spatial coverage are neglected.

In the North Atlantic Ocean, Woosley et al. (2016) found a significant increase in C_{ant} storage rates from 1.9 ± 0.4 Pg C dec^{-1} for the 1989–2003 period to 4.4 ± 0.9 Pg C dec^{-1} for 2003–2014. While the latter estimate is indistinguishable from our storage rate for the 2004–2014 decade (3.9 ± 0.4 Pg C dec^{-1}), their sink estimate for the first period is drastically lower than ours for the 1994–2004 decade (4.8 ± 0.2 Pg C dec^{-1}). This leads to opposite interpretations of the North Atlantic as a C_{ant} sink that is strongly increasing (Woosley et al., 2016) or moderately decreasing (this study) in strength. The changes reported by Woosley et al. (2016) rely on the comparison to a previous study by Wanninkhof et al. (2010) and are based on the reoccupation of a single north-south transect (A16) which covers the eastern basin of the North Atlantic Ocean. Thus, one likely cause for the different findings lies in their use of a single section in contrast to our use of data from all available cruises. Studies that compared ΔC_{ant} estimates for the Atlantic Ocean based on the analysis of single vs multiple reoccupied cruise lines indeed found that the inventories for whole hemispheric basins differ by around 30% (Gao et al., 2022; Woosley et al., 2016), which was attributed to insufficient observational coverage of east-west ΔC_{ant} gradients (Fig.1) by a single north-south oriented hydrographic section. Another reason why our inventories may differ from the regional analysis is the integration depth. While our study provides integrals over the top 3000m, Woosley et al. (2016) restricted their inventory calculation to water masses with ΔC_{ant} exceeding 3 µmol kg^{-1}, a threshold that is mostly located shallower than 2000m along the A16 section in the North Atlantic. Indeed, the depth layers that contribute to the decadal decrease of our inventories range from 1500 to 3000m (Fig. 3B). In contrast, our inventories over the top 1000m also show a tendency towards slightly higher C_{ant} storage changes in the more recent decade. Thus, whether we interpret the sink strength of the North Atlantic as increasing or decreasing depends among others on the chosen integration threshold.

For the South Atlantic Ocean, Woosley et al. (2016) reported a rather steady uptake rate (3.7 ± 0.8 and 3.2 ± 0.7 Pg C dec^{-1}) based on the analysis of a single reoccupied cruise section (A16S). In contrast, Gao et al. (2022) found that the rate of C_{ant} storage accelerated from 3.1 ± 0.2 Pg C dec^{-1} for the 1989–2005 period to 4.9 ± 0.3 Pg C dec^{-1} for the 2005–2013 period when extrapolating from the same A16S section to the whole South Atlantic basin. The most important difference between these two regional studies is again the choice of the vertical integration depth. While Woosley et al. (2016) restricted their

inventory calculation to ΔC_{ant} exceeding 3 µmol kg^{-1}, Gao et al. (2022) provided upon request integrated ΔC_{ant} over the top 3000 m (H. Gao and W.-J. Cai, pers. comm.). Our storage rates determined for the two decades of our analysis (3.9 ± 0.5 and 5.4 ± 0.6 Pg C dec^{-1}) agree with the regional estimates in the ranges of their uncertainty, but support the finding of an increasing rather than a constant or moderately decreasing basin wide storage rate. When interpreting the regional inventories in the Atlantic Ocean, it should be noted that the uncertainties provided by Woosley et al. (2016) are bulk uncertainties representing 20% of the absolute values, while those of Gao et al. (2022) are based on the latitudinal variability of column inventory estimates within 10° latitude bins. Neither uncertainty range is directly comparable to ours.

For the Pacific Ocean, the most recent regional study found that the basin-wide storage of C_{ant} over the top 1500 m accelerated from the first to the second decade of the 1995 to 2015 period (Carter et al., 2019). This increase was detected primarily in the Southern Hemisphere, where the ΔC_{ant} inventory increased from 5.4 ± 0.6 Pg C dec^{-1} (1995–2005) to 7.8 ± 0.6 Pg C dec^{-1} (2005–2015). In contrast, the Northern Hemisphere revealed a rather steady sink strength during these two periods (3.4 ± 0.5 and 4.0 ± 0.5 Pg C dec^{-1}). Within the Southern Hemisphere, the accelerated C_{ant} storage in the recent decade was found primarily on the equatorward side of the Southern Hemisphere Subtropical Gyre. This pattern is consistent with the slightly higher zonal mean content of ΔC_{ant} (around +2 µmol kg^{-1} dec^{-1}) that we find for our second decade (2004–2014) in the upper 1000m between the equator and 30°S (Fig. 3). Likewise, our decadal ΔC_{ant} inventories over the top 3000m in the South (8.6 ± 1.2 and 7.4 ± 1.0 Pg C dec^{-1}) and North Pacific (2.9 ± 0.8 to 3.2 ± 1.8 Pg C dec^{-1}) are similar to those of Carter et al. (2019). However, we do find an insignificant slow-down rather than an acceleration of the C_{ant} storage changes in the South Pacific, due to our higher storage changes during the first decade. This is partly due to our integration across small negative decadal differences in ΔC_{ant} located between 1500–3000m (Fig. 2B), a depth range which was not considered by Carter et al. (2019). In addition, there are notable differences in the observations incorporated in our analysis. In this study, we do not use the P16 cruise from 1991 due to missing TA data, but we do use calculated TA data from the South East Pacific in the 1990s (Fig. 1 and Table S1). The calculated TA data were adjusted by +3 µmol kg^{-1} according to crossover analysis with directly measured TA data. This positive adjustment of TA data from the 1990s sampling period increases our South Pacific ΔC_{ant} inventory for the 1994–2004 decade by about 1 Pg C (Fig. S11). The most important differences, however, is our consideration of TA for the calculation of C*, whereas Carter et al. (2019) derived C* from DIC by accounting for the effect of organic matter production and remineralization through changes in the oxygen content, but neglected TA changes due to the formation or dissolution of calcium carbonate minerals. If we remove TA from our C* calculation as well, this reduces the ΔC_{ant} column inventories (Fig. S11) and leads to an inventory that is about 3 Pg C dec^{-1} lower in the South Pacific for the 1994–2004 decade. However, according to our reassessment of the GLODAP crossover (Fig. S3) we do not have clear indications that this difference might primarily be due to data inconsistencies. We thus conclude that it might capture a real signal in the calcium carbonate cycle.

For the Indian Ocean, no multi-decadal regional studies are available for comparison to our ΔC_{ant} inventories (7.2 ± 0.9 and 5.7 ± 0.6 Pg C). Still, our inventories agree with the expected steady-state storage change (Fig. 5) based on the total C_{ant} inventory determined for the mid-1990s (Sabine et al., 2004, 1999). An intensified C_{ant} storage was previously described

for the decade around 2000, albeit based on a single reoccupied east-west section at around 20° and without deriving a whole basin ΔC_{ant} inventory (Murata et al., 2010). This is in agreement with our elevated reconstructed ΔC_{ant} inventories for our first decade 1994 – 2004.

We conclude from this comparison that the patterns and trends in our ΔC_{ant} reconstructions agree with those determined in regional studies, and that differences can — where they exist — be attributed to differences in the chosen integration depth, differences in the definition of the target variable C*, and sometimes most likely also to the uncertainty associated with the computation of a whole basin inventory from a single reoccupied transect (Woosley et al., 2016; Gao et al., 2022).

References of supplementary material

Bittig, H. C., Steinhoff, T., Claustre, H., Fiedler, B., Williams, N. L., Sauzède, R., Körtzinger, A., and Gattuso, J.-P.: An Alternative to Static Climatologies: Robust Estimation of Open Ocean CO2 Variables and Nutrient Concentrations From T, S, and O2 Data Using Bayesian Neural Networks, Front. Mar. Sci., 5, https://doi.org/10.3389/fmars.2018.00328, 2018.

Carter, B. R., Feely, R. A., Wanninkhof, R., Kouketsu, S., Sonnerup, R. E., Pardo, P. C., Sabine, C. L., Johnson, G. C., Sloyan, B. M., Murata, A., Mecking, S., Tilbrook, B., Speer, K., Talley, L. D., Millero, F. J., Wijffels, S. E., Macdonald, A. M., Gruber, N., and Bullister, J. L.: Pacific Anthropogenic Carbon Between 1991 and 2017, Glob. Biogeochem. Cycles, 2018GB006154, https://doi.org/10.1029/2018GB006154, 2019.

Clement, D. and Gruber, N.: The eMLR(C*) Method to Determine Decadal Changes in the Global Ocean Storage of Anthropogenic CO_2, Glob. Biogeochem. Cycles, 32, 654–679, https://doi.org/10.1002/2017GB005819, 2018.

Dlugokencky, E. and Tans, P.: Trends in atmospheric carbon dioxide, National Oceanic & Atmospheric Administration, Earth System Research Laboratory (NOAA/ESRL), 2019.

Doney, S. C., Lima, I., Feely, R. A., Glover, D. M., Lindsay, K., Mahowald, N., Moore, J. K., and Wanninkhof, R.: Mechanisms governing interannual variability in upper-ocean inorganic carbon system and air–sea CO2 fluxes: Physical climate and atmospheric dust, Deep Sea Res. Part II Top. Stud. Oceanogr., 56, 640–655, https://doi.org/10.1016/j.dsr2.2008.12.006, 2009.

Fong, M. B. and Dickson, A. G.: Insights from GO-SHIP hydrography data into the thermodynamic consistency of CO2 system measurements in seawater, Mar. Chem., 211, 52–63, https://doi.org/10.1016/j.marchem.2019.03.006, 2019.

Gao, H., Cai, W.-J., Jin, M., Dong, C., and Timmerman, A. H. V.: Ocean Ventilation Controls the Contrasting Anthropogenic CO2 Uptake Rates Between the Western and Eastern South Atlantic Ocean Basins, Glob. Biogeochem. Cycles, 36, e2021GB007265, https://doi.org/10.1029/2021GB007265, 2022.

Garcia, H. E., Boyer, T., Baranova, O. K., Locarnini, R., Mishonov, A., Grodsky, A., Paver, C., Weathers, K., Smolyar, I., Reagan, J., Seidov, D., and Zweng, M. M.: World Ocean Atlas 2018: Product Documentation. A. Mishonov, Technical Editor., 2019.

Gregor, L. and Gruber, N.: OceanSODA-ETHZ: a global gridded data set of the surface ocean carbonate system for seasonal to decadal studies of ocean acidification, Earth Syst. Sci. Data, 13, 777–808, https://doi.org/10.5194/essd-13-777-2021, 2021.

Gruber, N., Clement, D., Carter, B. R., Feely, R. A., van Heuven, S., Hoppema, M., Ishii, M., Key, R. M., Kozyr, A., Lauvset, S. K., Lo Monaco, C., Mathis, J. T., Murata, A., Olsen, A., Perez, F. F., Sabine, C. L., Tanhua, T., and Wanninkhof, R.: The oceanic sink for anthropogenic CO2 from 1994 to 2007, Science, 363, 1193–1199, https://doi.org/10.1126/science.aau5153, 2019.

Jackett, D. R. and McDougall, T. J.: A Neutral Density Variable for the World's Oceans, J. Phys. Oceanogr., 27, 27, 1997.

Johnson, K. M., Dickson, A. G., Eischeid, G., Goyet, C., Guenther, P., Key, R. M., Millero, F. J., Purkerson, D., Sabine, C. L., Schottle, R. G., Wallace, D. W. R., Wilke, R. J., and Winn, C. D.: Coulometric total carbon dioxide analysis for marine studies: assessment of the quality of total inorganic carbon measurements made during the US Indian Ocean CO2 Survey 1994–1996, Mar. Chem., 63, 21–37, https://doi.org/10.1016/S0304-4203(98)00048-6, 1998.

Johnson, K. M., Dickson, A. G., Eischeid, G., Goyet, C., Guenther, P. R., Key, R. M., Lee, K., Lewis, E. R., Millero, F. J., Purkerson, D. G., Sabine, C. L., Schottle, R. G., Wallace, D. W. R., Wilke, R. J., and Winn, C. D.: Carbon Dioxide, Hydrographic and Chemical Data Obtained During the Nine R/V Knorr Cruises Comprising the Indian Ocean CO2 Survey (WOCE Sections I8SI9S, I9N, I8NI5E, I3, I5WI4, I7N, I1, I10, and I2, and 12; December 1, I994-January 22, 1996), https://doi.org/10.3334/CDIAC/OTG.NDP080, 2002.

Key, R. M., Kozyr, A., Sabine, C. L., Lee, K., Wanninkhof, R., Bullister, J. L., Feely, R. A., Millero, F. J., Mordy, C., and Peng, T.-H.: A global ocean carbon climatology: Results from Global Data Analysis Project (GLODAP), Glob. Biogeochem. Cycles, 18, https://doi.org/10.1029/2004GB002247, 2004.

Lauvset, S. K., Key, R. M., Olsen, A., van Heuven, S., Velo, A., Lin, X., Schirnick, C., Kozyr, A., Tanhua, T., Hoppema, M., Jutterström, S., Steinfeldt, R., Jeansson, E., Ishii, M., Perez, F. F., Suzuki, T., and Watelet, S.: A new global interior ocean mapped climatology: the 1◦ × 1◦ GLODAP version 2, 16, 2016.

Lauvset, S. K., Lange, N., Tanhua, T., Bittig, H. C., Olsen, A., Kozyr, A., Álvarez, M., Becker, S., Brown, P. J., Carter, B. R., Cotrim da Cunha, L., Feely, R. A., van Heuven, S., Hoppema, M., Ishii, M., Jeansson, E., Jutterström, S., Jones, S. D., Karlsen, M. K., Lo Monaco, C., Michaelis, P., Murata, A., Pérez, F. F., Pfeil, B., Schirnick, C., Steinfeldt, R., Suzuki, T., Tilbrook, B., Velo, A., Wanninkhof, R., Woosley, R. J., and Key, R. M.: An updated version of the global interior ocean biogeochemical data product, GLODAPv2.2021, Earth Syst. Sci. Data, 13, 5565–5589, https://doi.org/10.5194/essd-13-5565-2021, 2021.

Lauvset, S. K., Lange, N., Tanhua, T., Bittig, H. C., Olsen, A., Kozyr, A., Alin, S., Álvarez, M., Azetsu-Scott, K., Barbero, L., Becker, S., Brown, P. J., Carter, B. R., da Cunha, L. C., Feely, R. A., Hoppema, M., Humphreys, M. P., Ishii, M., Jeansson, E., Jiang, L.-Q., Jones, S. D., Lo Monaco, C., Murata, A., Müller, J. D., Pérez, F. F., Pfeil, B., Schirnick, C., Steinfeldt, R., Suzuki, T., Tilbrook, B., Ulfsbo, A., Velo, A., Woosley, R. J., and Key, R. M.: GLODAPv2.2022: the latest version of the global interior ocean biogeochemical data product, Earth Syst. Sci. Data, 14, 5543–5572, https://doi.org/10.5194/essd-14-5543-2022, 2022.

Locarnini, R., Mishonov, A., Baranova, O., Boyer, T., Zweng, M., Garcia, H., Reagan, J., Seidov, D., Weathers, K., Paver, C., Smolyar, I., and Locarnini, R.: World Ocean Atlas 2018, Volume 1: Temperature, 2019.

Millero, F. J., Dickson, A. G., Eischeid, G., Goyet, C., Guenther, P., Johnson, K. M., Key, R. M., Lee, K., Purkerson, D., Sabine, C. L., Schottle, R. G., Wallace, D. W. R., Lewis, E., and Winn, C. D.: Assessment of the quality of the shipboard measurements of total alkalinity on the WOCE Hydrographic Program Indian Ocean CO2 survey cruises 1994–1996, Mar. Chem., 63, 9–20, https://doi.org/10.1016/S0304-4203(98)00043-7, 1998.

Murata, A., Kumamoto, Y., Sasaki, K., Watanabe, S., and Fukasawa, M.: Decadal increases in anthropogenic CO2 along 20°S in the South Indian Ocean, J. Geophys. Res. Oceans, 115, https://doi.org/10.1029/2010JC006250, 2010.

Olsen, A., Key, R. M., van Heuven, S., Lauvset, S. K., Velo, A., Lin, X., Schirnick, C., Kozyr, A., Tanhua, T., Hoppema, M., Jutterström, S., Steinfeldt, R., Jeansson, E., Ishii, M., Pérez, F. F., and Suzuki, T.: The Global Ocean Data Analysis Project version 2 (GLODAPv2) – an internallyconsistent data product for the world ocean, Earth Syst. Sci. Data, 8, 297–323, https://doi.org/10.5194/essd-8-297-2016, 2016.

Poulter, B., Bastos, A., Canadell, J., Ciais, P., Gruber, N., Hauck, J., Jackson, R., Ishii, M., Müller, Jens Daniel, J., Patra, P., and Tian, H.: Inventorying Earth's Land and Ocean Greenhouse Gases, Eos, 103, https://doi.org/10.1029/2022eo179084, 2022.

Sabine, C. L., Key, R. M., Johnson, K. M., Millero, F. J., Poisson, A., Sarmiento, J. L., Wallace, D. W. R., and Winn, C. D.: Anthropogenic CO2 inventory of the Indian Ocean, Glob. Biogeochem. Cycles, 13, 179–198, https://doi.org/10.1029/1998GB900022, 1999.

Sabine, C. L., Feely, R. A., Gruber, N., Key, R. M., Lee, K., Bullister, J. L., Wanninkhof, R., Wong, C. S., Wallace, D. W. R., Tilbrook, B., Millero, F. J., Peng, T.-H., Kozyr, A., Ono, T., and Rios, A. F.: The Oceanic Sink for Anthropogenic CO2, Science, 305, 367–371, https://doi.org/10.1126/science.1097403, 2004.

Tsujino, H., Urakawa, S., Nakano, H., Small, R. J., Kim, W. M., Yeager, S. G., Danabasoglu, G., Suzuki, T., Bamber, J. L., Bentsen, M., Böning, C. W., Bozec, A., Chassignet, E. P., Curchitser, E., Boeira Dias, F., Durack, P. J., Griffies, S. M., Harada, Y., Ilicak, M., Josey, S. A., Kobayashi, C., Kobayashi, S., Komuro, Y., Large, W. G., Le Sommer, J., Marsland, S. J., Masina, S., Scheinert, M.,

Tomita, H., Valdivieso, M., and Yamazaki, D.: JRA-55 based surface dataset for driving ocean–sea-ice models (JRA55-do), Ocean Model., 130, 79–139, https://doi.org/10.1016/j.ocemod.2018.07.002, 2018.

Wanninkhof, R., Doney, S. C., Bullister, J. L., Levine, N. M., Warner, M., and Gruber, N.: Detecting anthropogenic CO2 changes in the interior Atlantic Ocean between 1989 and 2005, J. Geophys. Res. Oceans, 115, https://doi.org/10.1029/2010JC006251, 2010.

Woosley, R. J., Millero, F. J., and Wanninkhof, R.: Rapid anthropogenic changes in CO2 and pH in the Atlantic Ocean: 2003–2014, Glob. Biogeochem. Cycles, 30, 70–90, https://doi.org/10.1002/2015GB005248, 2016.

Zweng, M. M., Reagan, J., Seidov, D., Boyer, T., Locarnini, R., Garcia, H., Mishonov, A., Baranova, O. K., Paver, C., and Smolyar, I.: WORLD OCEAN ATLAS 2018 Volume 2: Salinity, 2019.